iScience

Article

Severe acute respiratory syndrome coronavirus 2 infection unevenly impacts metabolism in the coronal periphery of the lungs

Graphical abstract

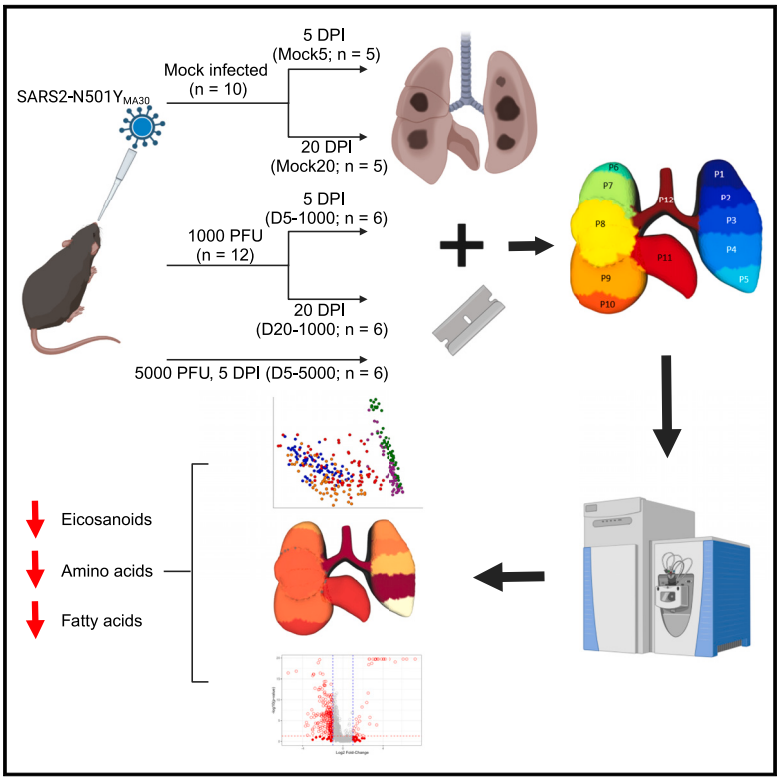

Highlights

- COVID-19 significantly decreases amino acids, fatty acids, and most eicosanoids
- SARS-CoV-2 preferentially localizes to central lung tissue
- Metabolic disturbance is highest in peripheral tissue, not central as for viral load
- Spatial metabolomics allows the detection of metabolites not altered overall

Authors

Jarrod Laro, Biyun Xue, Jian Zheng, Monica Ness, Stanley Perlman, Laura-Isobel McCall

Correspondence

lmccall@sdsu.edu

In brief

Immunology; Human metabolism

Laro et al., 2025, iScience *28*, 111727
February 21, 2025
https://doi.org/10.1016/j.isci.2024.111727

CellPress

iScience

CellPress
OPEN ACCESS

Article

Severe acute respiratory syndrome coronavirus 2 infection unevenly impacts metabolism in the coronal periphery of the lungs

Jarrod Laro,[1,2,4] Biyun Xue,[3,4] Jian Zheng,[3] Monica Ness,[1,2] Stanley Perlman,[3] and Laura-Isobel McCall[1,2,5,*]
[1]Department of Chemistry and Biochemistry, University of Oklahoma, Norman, OK 73019, USA
[2]Department of Chemistry and Biochemistry, San Diego State University, San Diego, CA 92182, USA
[3]Department of Microbiology and Immunology, University of Iowa, Iowa City, IA 52242, USA
[4]These authors contributed equally
[5]Lead contact
*Correspondence: lmccall@sdsu.edu
https://doi.org/10.1016/j.isci.2024.111727

SUMMARY

SARS-CoV-2, the virus responsible for COVID-19, is a highly contagious virus that can lead to hospitalization and death. COVID-19 is characterized by its involvement in the lungs, particularly the lower lobes. To improve patient outcomes and treatment options, a better understanding of how SARS-CoV-2 impacts the body, particularly the lower respiratory system, is required. In this study, we sought to understand the spatial impact of COVID-19 on the lungs of mice infected with mouse-adapted SARS2-N501Y$_{MA30}$. Overall, infection caused a decrease in fatty acids, amino acids, and most eicosanoids. When analyzed by segment, viral loads were highest in central lung tissue, while metabolic disturbance was highest in peripheral tissue. Infected peripheral lung tissue was characterized by lower levels of fatty acids and amino acids when compared to central lung tissue. This study highlights the spatial impacts of SARS-CoV-2 and helps explain why peripheral lung tissue is most damaged by COVID-19.

INTRODUCTION

Severe acute respiratory syndrome coronavirus 2 (SARS-CoV-2) is a respiratory virus that causes coronavirus disease 2019 (COVID-19). COVID-19 can have a wide range of severity: some patients remain asymptomatic while others experience mild symptoms such as fatigue, nausea, and a loss of taste and smell. In dire cases, patients experience hypoxia and acute respiratory disease syndrome (ARDS), which can ultimately lead to death. Indeed, by the end of 2023, the World Health Organization recorded over 700 million cases of COVID-19 worldwide, with 7 million deaths being attributed directly to the infection or its complications.[1] SARS-CoV-2 is highly contagious and mutates rapidly, explaining its continued prevalence and appearance of new variants despite the widespread availability of vaccines.[2] Even after acute SARS-CoV-2 infection resolves, a substantial fraction of patients report continued fatigue, breathlessness, chest pains, and the onset of conditions such as type 2 diabetes and postural orthostatic tachycardia syndrome (POTS).[3,4] These post-acute sequelae, most commonly referred to as "long COVID," are poorly characterized, with little understanding of why they occur, how to effectively diagnose them, or how to prevent them.[5] Due to its continued presence, it is crucial to understand how SARS-CoV-2 impacts the host, particularly the lower respiratory system, to improve patient outcomes and to develop better treatments and prophylactics.

The metabolome, the collection of molecules with a molecular weight under 1500 Da present in an organism, is extremely sensitive to small changes caused by age, gender, sex, diet, illness, and so forth, making analysis of the metabolome a useful tool for understanding the impact and mechanism of disease.[6] Typically, metabolomic studies investigate a biofluid, a small sampling of an organ, or the organ as a whole. The study of the serum metabolome has been helpful in discerning some of the impacts of conditions such as Chagas Disease, influenza, and COVID-19, but the study of biofluids is unable to capture the heterogeneity present within organs.[7,8] Indeed, metabolomic studies that have segmented the heart, lungs, liver, et cetera, have identified differences in metabolism between parts of the same organ.[9–12] While SARS-CoV-2 primarily targets the lungs, the specific affected lung segments can vary based on the patient. Tissue damage can present in a single lobe of the lung or all lobes, be peripherally or centrally distributed in the transversal plane, and cause ground glass opacities or consolidations.[13–16] Despite the heterogeneous presentation of the condition, the lower segments of the coronal plane are the ones most commonly impacted by SARS-CoV-2 in humans, with the majority of cases showing abnormalities in the periphery of the transverse plane of these segments.[14,16–18] While many studies have examined the impact of COVID-19 on the metabolome (e.g.,[19–22]), none have attempted to explain the localized impact of SARS-CoV-2 through the use of spatial metabolomics. Additionally, due to its ease of

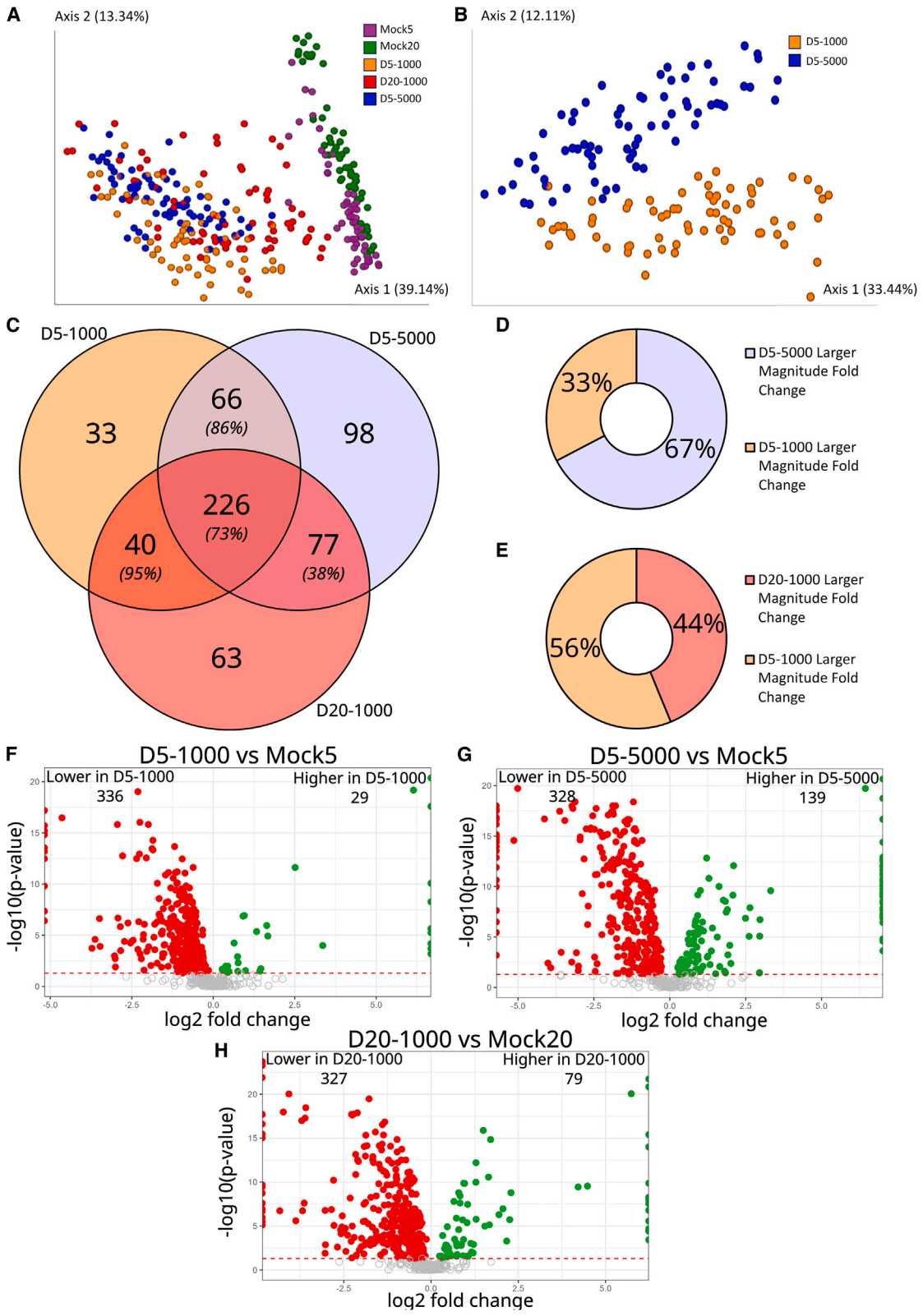

(legend on next page)

collection in clinical settings, the majority of COVID-19 studies focus on common biofluids such as plasma and urine (for example,[23–27]). While plasma provides information on the biological system as a whole, it cannot capture localized, distinct effects of a condition within individual organs.

To address these gaps, we investigated the impact of COVID-19 by performing a systematic spatial metabolomic analysis of lung tissues from mice infected with the mouse-adapted SARS2-N501Y$_{MA30}$ strain[28] at a sublethal or lethal dose (1000 plaque-forming units and 5000 plaque-forming units, respectively) to mimic different levels of COVID-19 severity five days post-infection (DPI). To identify potential markers of post-acute sequelae, we analyzed lung tissues twenty days post-infection from mice infected with 1000 plaque-forming units. Through this approach, we identified localized effects of COVID-19 on the lung metabolism and preferential localization of SARS-CoV-2 in mouse lung tissue.

RESULTS

Severe acute respiratory syndrome coronavirus 2 infection causes substantial metabolic changes that persist at least 20 days after infection

To examine the impact of COVID-19 on lung metabolism, five experimental groups were used: mock-infected mice euthanized 5 DPI (Mock5) or 20 DPI (Mock20), mice infected with 1000 or 5000 plaque-forming units of SARS2-N501Y$_{MA30}$ and euthanized 5 DPI (D5-1000 and D5-5000), and mice infected with 1000 plaque-forming units of SARS2-N501Y$_{MA30}$ and euthanized 20 DPI (D20-1000). Initially, the overall metabolic differences between each disease state were analyzed irrespective of lung position. We observed that the mock-infected mice possessed strong metabolic differences from infected mice (Figure 1A; Pseudo-F > 60 for D5-1000, D5-5000, and D20-2000 when compared to the time-matched mock-infected control). D5-5000 demonstrated the largest metabolic perturbation relative to their time-matched mock-infected control, followed by D5-1000 and D20-1000 (Figure S1). D5-1000 and D5-5000 mice also displayed strong metabolic differences from each other (Pseudo-F = 23.1, q-value <0.001), made more apparent when analyzing only those two groups (Figure 1B). While D20-1000 mice had clear metabolic differences from mock-infected mice, they displayed a wide range of metabolome profiles, with some individual mice clustering closer to uninfected mice while others clustered with the D5-1000 and D5-5000 mice (Figure 1A; Figure S2A). Metabolic differences between mice were not clearly associated with viral load measured from lung tissue (Figure S3).

Severe acute respiratory syndrome coronavirus 2 infection decreases major molecular families in the lung

To identify individual metabolites impacted by COVID-19, *p*-values were calculated by comparing each infected group with their time-matched mock-infected control and then false-discovery rate (FDR) adjusted; fold change values for each disease state were calculated by dividing the median total ion current (TIC) normalized signal intensity of the metabolite in the infected group by the median TIC-normalized signal intensity of the metabolite in the time-matched mock-infected controls. The majority of significantly altered metabolites (FDR-adjusted *p*-value <0.05) were shared between all three disease states (Figure 1C). Overall, metabolites affected under all three infection conditions, shared between D5-1000 and D20-1000 or shared between D5-1000 and D5-5000, predominantly showed the same direction of change, highlighting the reproducibility of the metabolic impact of infection. Fold change differences to the time-matched mock-infected control were more pronounced for two-thirds of the metabolites significantly impacted in D5-5000 mice when compared to D5-1000 mice (Figure 1D; χ^2 = 30.488, *p*-value <0.00001). No significant difference was observed between the magnitude of the fold change differences in D5-1000 mice versus D20-1000 mice (Figure 1E; χ^2 = 3.613, *p*-value = 0.06). The majority of significantly altered metabolites exhibited a decrease relative to the mock control, with 92%, 70%, and 81% of metabolites showing a significant decrease in D5-1000, D5-5000, and D20-1000 mice respectively, compared to time-matched mock-infected controls (Figures 1F–1H). Overall, infected lung tissue across all states had significantly altered levels of amino acids, fatty acids, eicosanoids, acylcarnitines, and purines, among other molecular families (Figures 2A–2C).

Amino acids were decreased across all disease states (Figures 2A–2D). D5-1000 mice exhibited significantly lower levels of glutamate, methionine, and arginine compared to mock-infected controls; in addition to those amino acids, D5-5000 mice had significantly lower levels of threonine, tyrosine, phenylalanine, and tryptophan compared to mock-infected controls. D20-1000 mice had a significant decrease in threonine, glutamate, tyrosine, and arginine. Alongside the decrease in tryptophan levels observed in D5-5000 mice, there was a significant increase in the levels of kynurenine, a well-characterized

Figure 1. SARS-CoV-2 infected mice show strong metabolic differences from mock-infected mice overall in the lungs

(A) Principal coordinate analysis for all infection states across the 12 lung segments for each mouse (Mock-infected groups - *n* = 5 mice; 59 lung sections. Infected groups - *n* = 6 mice; D5-1000 = 69 lung sections, D5-5000 = 72 sections, D20-1000 = 71 sections).

(B) Principal coordinate analysis for D5-1000 vs. D5-5000.

(C) Overlap of the metabolites significantly impacted in each of the infected groups when compared to timepoint-matched mock-infected controls. Italicized percentages in each overlap are the percentage of metabolites that have the same direction of change.

(D) Comparison of the magnitude of log2 fold changes between annotated, significant metabolites in both D5-5000 and D5-1000 mice that have the same direction of fold change (*n* = 254 metabolites).

(E) Comparison of the magnitude of log2 fold change between annotated, significant metabolites in both D20-1000 and D5-1000 mice that have the same direction of fold change (*n* = 217 metabolites).

(F–H) Volcano plots of annotated metabolites for (F) D5-1000, (G) D5-5000, (H) and D20-1000 groups compared to timepoint-matched mock-infected controls. Significant metabolites (FDR-adjusted *p*-value <0.05) are filled-in, colored data points. Red dots, fold change<1, and green dots, fold change> 1. Gray, unfilled data points are metabolite features that were not significantly different. Also see Figures S1–S3.

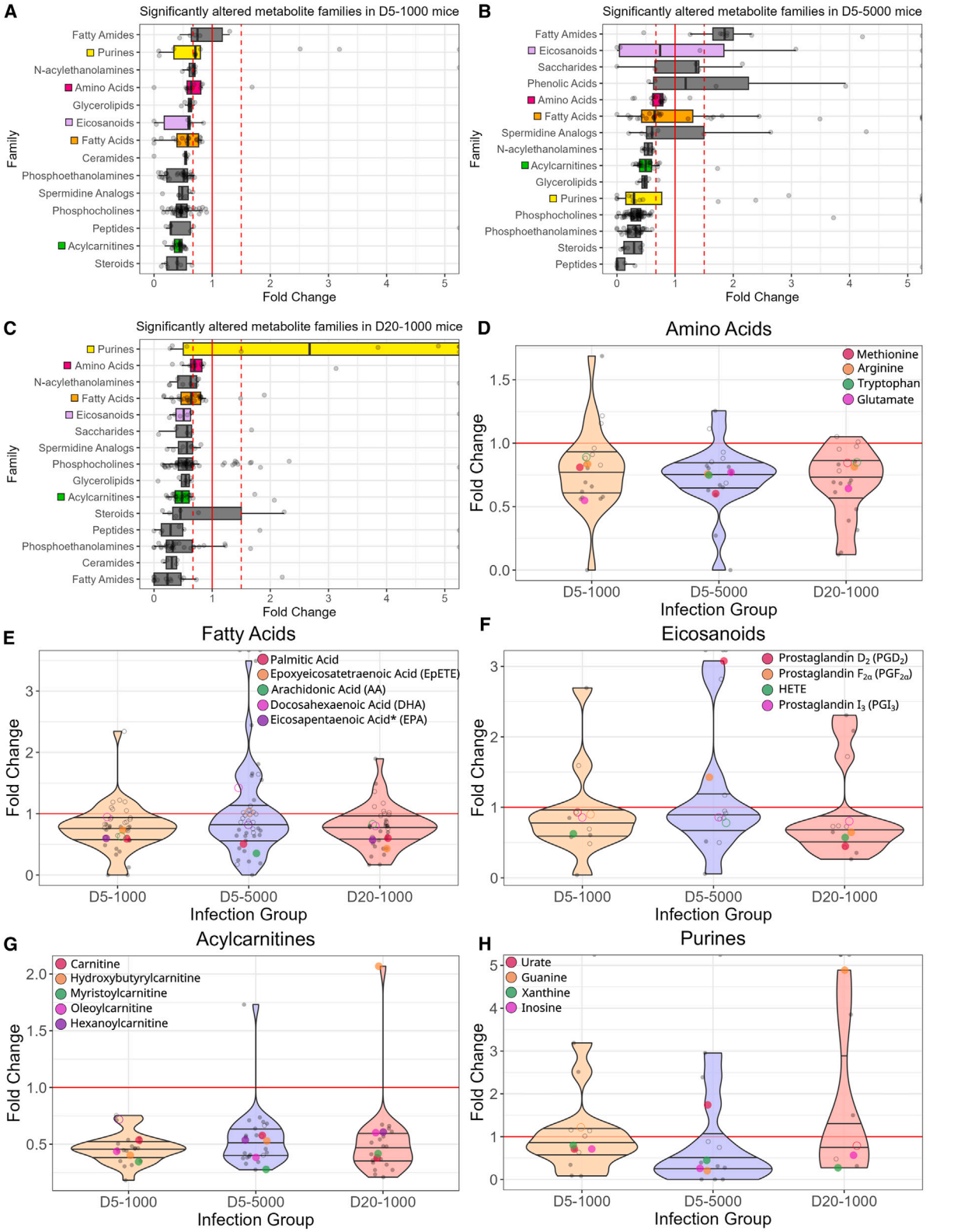

(legend on next page)

sign of inflammation due to the activation of the TDO2/IDO1-catalyzed transformation of tryptophan into kynurenine.[29] Kynurenine was not significantly increased in either D5-1000 or D20-1000 mice, implying lower levels of inflammation and disease severity in these groups (Figure S4).

Fatty acid metabolism was significantly impacted in all disease states (Figures 2A–2C and 2E). Palmitic acid (PA) and epoxyeicosatetraenoic acid (EpETE) were both lower in D5-1000 mice and D20-1000 mice compared to mock-infected controls. *m/z* 303.23 RT 3.02 min, annotated as eicosapentaenoic acid (EPA) or an isomer (Figure S5) was also lower in D5-1000 mice and D20-1000 mice compared to mock-infected controls. PA and arachidonic acid (AA) were both significantly lower in D5-5000 mice, whereas EpETE and EPA were not significantly altered. Docosahexaenoic acid (DHA), a 22-carbon polyunsaturated ω-3 fatty acid with anti-inflammatory effects,[30–32] was not significantly altered in any disease state. 20-carbon polyunsaturated fatty acids such as AA and EPA serve as the precursor for eicosanoids, which play a key role in inflammatory responses.[33–36] Eicosanoid products of the ω-3 fatty acid EPA, such as prostaglandin I_3 (PGI_3), prostaglandin E_3, resolvins, and protectins, have anti-inflammatory effects that temper the effects of AA-derived eicosanoids.[32,37–40] Eicosanoids were generally decreased in D5-1000 and D20-1000 mice compared to timepoint-matched mock-infected controls but had larger fold changes in D5-5000 (Figure 2F). Multiple eicosanoids were only detected in D5-5000 tissue. Prostaglandin D_2 (PGD_2) and prostaglandin $F_{2\alpha}$ ($PGF_{2\alpha}$) were not significantly altered in D5-1000 mice but were significantly increased in D5-5000 mice and significantly decreased in D20-1000 mice compared to mock-infected controls. PGI_3 was detected but not significantly altered in overall lung tissue. Indeed, PGD_2 and $PGF_{2\alpha}$ had a significant, positive correlation with post-infection viral load while PGI_3 lacked any significant correlation (Table S1).

Acylcarnitines and their building block, carnitine, were almost ubiquitously lower across all three disease states (Figures 2A–2C and 2G). Significantly altered acylcarnitines include hexanoylcarnitine (C6, medium chain), myristoylcarnitine (C14, long chain), and oleoylcarnitine (C18:1, unsaturated long chain). Hydroxybutyrylcarnitine (C4, hydroxy short chain) was the only detected acylcarnitine with elevated levels at D20. The impact of SARS-CoV-2 infection did not appear to be acyl chain length specific. Acylcarnitines are crucial molecules for the transport of fatty acids across mitochondrial walls. Upon being transported into the mitochondria, fatty acids are able to be catabolized to produce energy.[41] Decreased levels of acylcarnitines in tandem with lower levels of several fatty acids could be a consequence of increased β-fatty acid oxidation for the production of energy for viral replication.

A significant impact on purine metabolism was observed in infected mice (Figures 2A–2C and 2H). Urate, the end product of purine metabolism, was significantly lower in D5-1000 mice, but significantly higher in D5-5000 mice compared to controls. Xanthine, guanine, and inosine were all significantly lower in D5-5000 mice. Interestingly, in D20-1000 mice, multiple adenosine analogs (adenosine monophosphate and deoxyadenosine monophosphate) and guanine/guanosine presented with fold change increases of up to 20-fold when compared to Mock20 mice or were only detected in the D20-1000 mice. When combining D5-1000 and D5-5000 mice, purines demonstrated a negative correlation with viral loads while urate had a positive correlation (Table S1).

Post-infection severe acute respiratory syndrome coronavirus 2 viral load does not correlate with the intensity of local metabolic disturbance

During the initial collection of lung tissue prior to metabolite extraction and LC-MS analysis, each lung was sectioned into 11 lung sections plus the trachea based on the biological segmentation of mouse lung lobes (Figures 3A and 3B; positions 1–5, left lung; positions 6–7, right superior lobe; position 8, right middle lobe; positions 9–10, right inferior lobe; position 11, post-caval lobe; position 12, trachea). Seeking to better understand the localization of COVID-19 effects, we categorized the 11 lung segments as either central or peripheral lung tissue. Lung segments P2-P4 and P7-P9 are from the central region of the lung, while segments P1, P5, P6, and P10 are from the peripheral region of the lung (Figure 3C). For this analysis, we did not include the post-caval mouse lung lobe (P11) due to a lack of a human analog. For all five experimental groups, there was a significant difference between the overall metabolome of the central positions and the peripheral positions, with D5-5000 mice showing the largest differences and Mock5 mice showing the smallest differences (Table S2). As expected, D5-5000 mice had significantly higher viral loads than D5-1000 and D20-1000 mice (Figure 3F; $p < 1.095e-11$; Table S3), matching the larger metabolic differences observed between D5-5000 mice and Mock5 mice. D5-1000 mice had significantly higher viral loads than D20-1000 mice (Figures 3D and 3H; $p = 0.007$; Table S3). Central lung tissue had a higher median viral load than peripheral lung tissue in all three disease states. Despite this, peripheral lung tissue had significantly higher levels of metabolic disturbance

Figure 2. SARS-CoV-2 infection decreases major molecular families in the lung

All data represented as median fold change.

(A–C) Significantly altered molecular families for (A) D5-1000, (B) D5-5000, and (C) D20-1000 mice compared to timepoint-matched mock-infected controls (Mock-infected groups - $n = 5$ mice; 59 lung sections. Infected groups - $n = 6$ mice; D5-1000 = 69 lung sections, D5-5000 = 72 sections, D20-1000 = 71 sections). All families depicted had at least 4 annotated metabolites belonging to that family. Dots on the right edge of each panel represent metabolites that had fold changes greater than 5. Dashed red lines represent a fold change of 0.67 or 1.5 while the solid red line represents a fold change of 1. Each filled dot represents a significantly impacted metabolite. Families visualized in panels D–H were colored to make them easier to observe between panels A–C. The upper hinge represents the 75th percentile, the middle line represents the 50th percentile, and the lower hinge represents the 25th percentile. Each whisker extends from its respective hinge by 1.5 times the interquartile range of the hinge.

(D–H) Violin plots of specific molecular families across all 3 disease states compared to timepoint matched mock-infected controls. Solid dots represent members of the family with an FDR-adjusted p-value <0.05 while hollow dots represent members of the family with an FDR-adjusted p-value >0.05. Red line, fold change of 1. From top to bottom, each line represents the 100th, 75th, 50th, 25th, and 0th percentile, respectively. Also see Figures S4, S5, and Table S1.

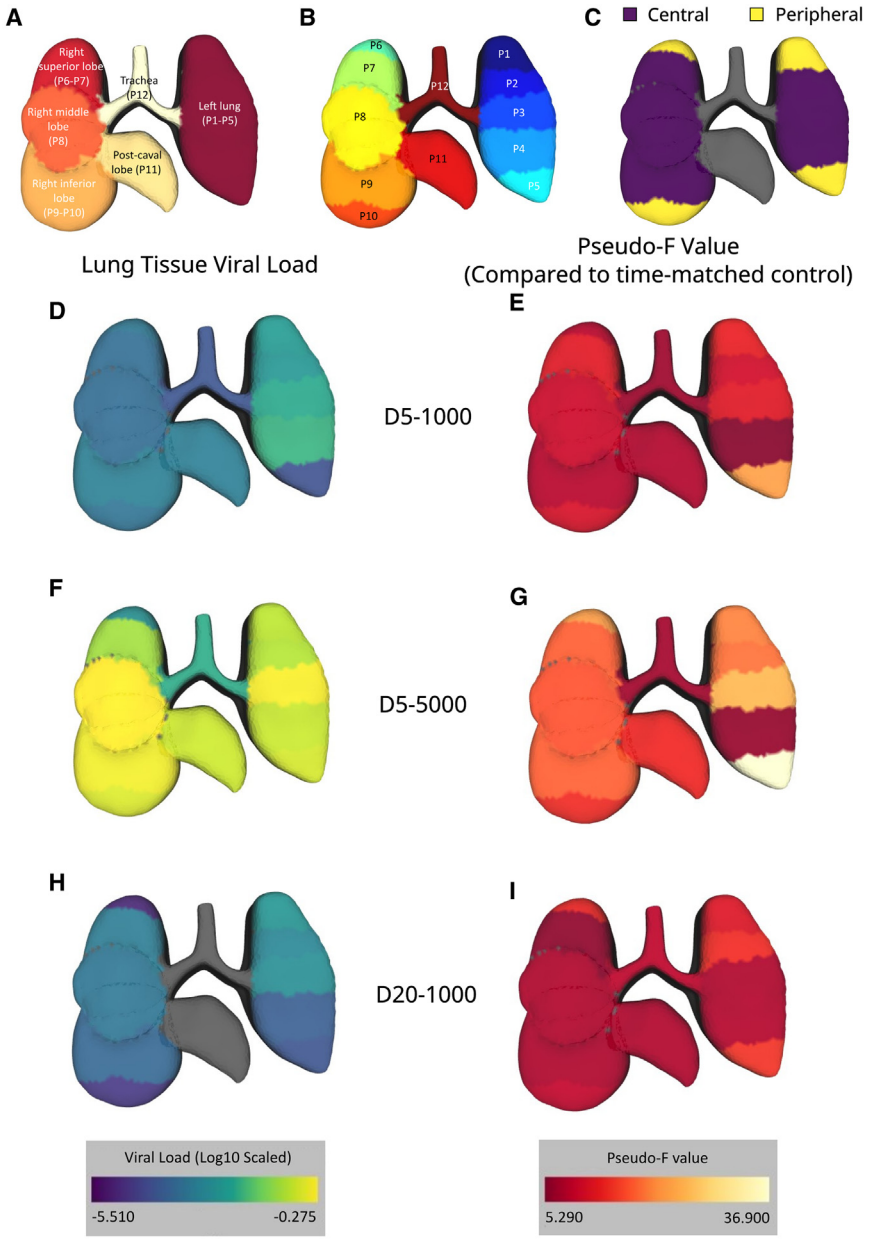

Figure 3. Spatial and temporal impact of SARS-CoV-2 infection on the lungs

(Mock-infected groups - n = 5 mice; 59 lung sections. Infected groups - n = 6 mice; D5-1000 = 69 lung sections, D5-5000 = 72 sections, D20-1000 = 71 sections).

(A) Biological segmentation of mouse lung lobes, one color per segment.

(B) Experimental segmentation approach for each mouse lung. Colors show the border between the segments.

(C) Classification of central (purple) vs. peripheral (yellow) lung segments in the coronal plane. Positions P11 and P12 are grayed out because they were not included in this analysis.

(D, F, and H) Log-transformed median viral loads as determined by qPCR of the N transcript, see STAR Methods, at each position for D5-1000 mice (D), D5-5000 mice (F), and D20-1000 mice (H). Gray lobes represent a median viral load of 0 (below the limit of detection). Common scale.

(E, G, and I) PERMANOVA pseudo-F values at each position of the lung. Pseudo-F values are a measure of the overall metabolic difference between samples, with larger values representing larger differences. Each color represents the pseudo-F value at each position between the infected samples and their respective time matched mock-infected sample at that position for D5-1000 mice (E), D5-5000 mice (G), and D20-1000 mice (I). Common scale. Raw data for D-I can be found in Table S3. Also see Figures S2, S6, and Tables S2–S5.

than central lung tissue in D5-1000 and D5-5000 (p = 0.007 and p = 0.03, respectively). In fact, there was no significant correlation between viral load and pseudo-F value (Figure S6). All infected lung positions had significant differences in metabolism when compared to their time-matched mock-infected controls (Figures 3E, 3G, and 3I; Table S3). When comparing D20-1000 to D5-1000 mice, upper lung segments (P1, P2, and P6-P8) did not show a statistically significant difference in metabolome and trended further away from mock-infected mice than lower lung segments, suggesting a slower recovery in the upper segments of the lungs (Figure S2B; Table S4). Additionally, lung segments located in the same relative positions on the left and right lungs (e.g., position P1 on the left lung and segment P6 on the right lung) exhibited remarkably similar metabolic profiles to each other in both infected and mock-infected mice (Table S5).

Severe acute respiratory syndrome coronavirus 2 infection has differential localized metabolic effects on the metabolome of peripheral and central lung tissue

To investigate the impact of COVID-19 on individual metabolites, fold difference and p-value calculations were performed on the mock-normalized signal intensities for peripheral vs. central lung segments. We then identified metabolites that had significantly different normalized fold differences between the peripheral and central lobes. D5-1000 mice had 111 significantly altered metabolites, D5-5000 mice had 216 significantly altered metabolites, and D20-1000 mice had 152 significantly altered metabolites (Figure 4A). 49%, 39%, and 48% of these metabolites, respectively, were only significantly altered when comparing peripheral tissue to central tissue and were not classified as significant when looking at the overall lung (Figures 4B–4D). While amino acids, fatty acids, eicosanoids, and purines were all significantly decreased by infection in overall D5-1000 lung tissue (Figures 2D–2F

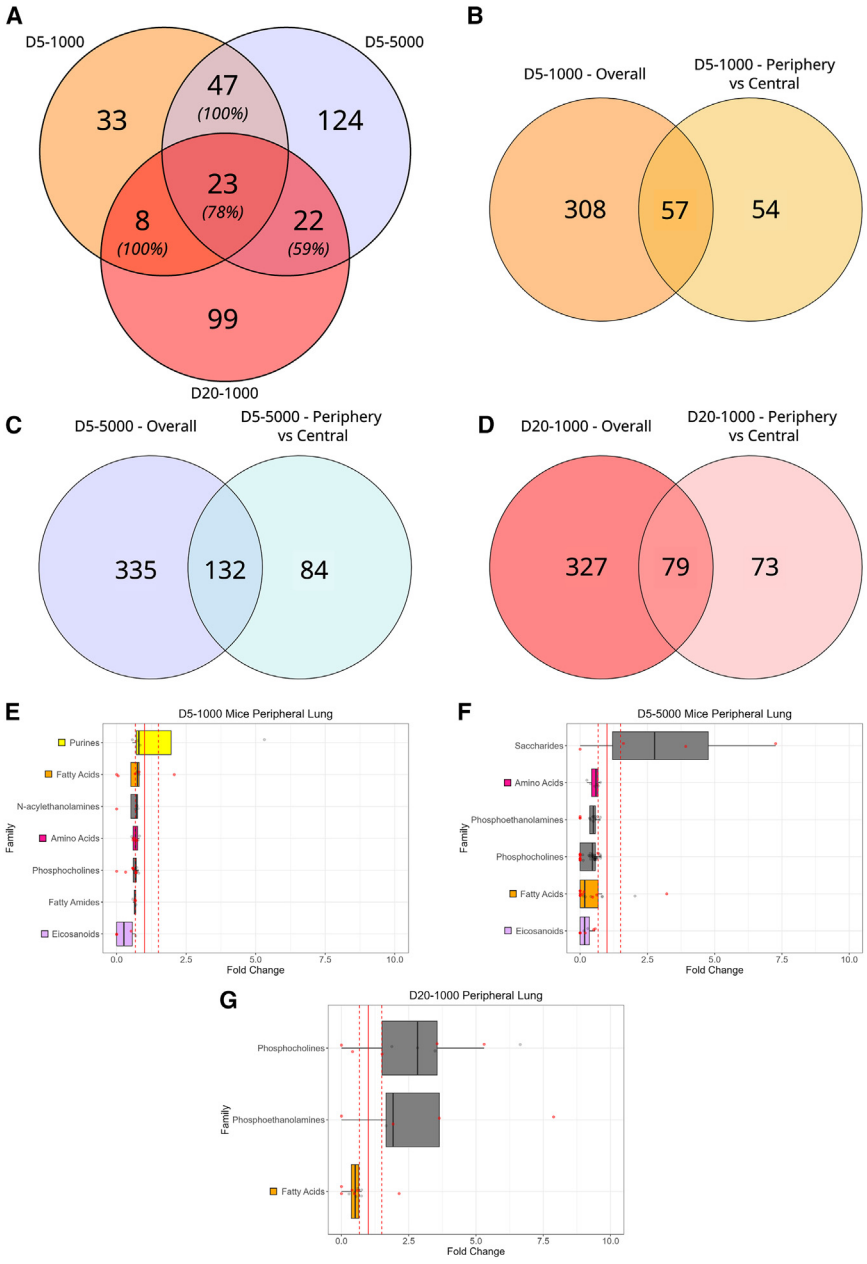

Figure 4. SARS-CoV-2 infection has differential localized metabolic effects on the metabolome of peripheral and central lung tissue

(Mock-infected groups - n = 5 mice; 59 lung sections. Infected groups - n = 6 mice; D5-1000 = 69 lung sections, D5-5000 = 72 sections, D20-1000 = 71 sections).

(A) Overlap of metabolites that are significantly different between peripheral and central lung tissue when normalized to their timepoint-matched mock-infected controls. Italicized percentages in each overlap are the percentage of metabolites that all have the same direction of change.

(B–D) Comparison of the metabolites that significantly differ between infected and uninfected mice without the consideration of position and metabolites that are significantly different between peripheral and central lung tissue when normalized to their timepoint-matched mock-infected controls in (B) D5-1000, (C) D5-5000, and (D) D20-1000.

(E–G) Significantly altered molecular families for the peripheral lung tissue of D5-1000 (E), D5-5000 (F), and D20-1000 (G) mice when normalized to their timepoint-matched mock-infected controls and when compared to central lung tissue. All families depicted had at least 4 members. Dashed red lines represent a fold change of 0.67 or 1.5 while the solid red line represents a fold change of 1. Individual family members that were not significantly different overall but were significantly different between the peripheral and central tissue are colored red while metabolites that were significantly different overall in addition to being significantly different between peripheral and central tissue are gray. Family colors as in Figure 2. All data represented as median fold change. The upper hinge represents the 75th percentile, the middle line represents the 50th percentile, and the lower hinge represents the 25th percentile. Each whisker extends from its respective hinge by 1.5 times the interquartile range of the hinge. Also, see Table S1.

and 2H), they were all significantly more decreased by infection in peripheral tissue when compared to central tissue (Figure 4E). Similarly, amino acids, fatty acids, and eicosanoids were more decreased by infection in the peripheral lung tissue of D5-5000 mice (Figure 4F), and fatty acids were more decreased in the peripheral lung tissue of D20-1000 mice (Figure 4G).

Levels of tryptophan (Figure 5A), tyrosine, and phenylalanine were all significantly more decreased by infection in peripheral lung segments than central lung segments in D5-1000 and D5-5000 mice. Prostaglandin I_3 (Figure 5B) and an unannotated arachidonic acid-derived prostaglandin (Figure 5C) were both significantly lower in the peripheral tissue of D5-1000 and D5-5000 mice. D5-5000 mice also had lower levels of $PGF_{2\alpha}$ and an unannotated eicosapentaenoic acid-derived prostaglandin in their peripheral tissue. Docosahexaenoic acid (Figure 5D) was significantly higher in peripheral tissue when compared to central tissue. The fatty amides palmitamide and octadecanamide (Figure 5E) were significantly lower in the peripheral tissue of D5-1000 and D5-5000 mice when compared to central tissue. Lastly, a number of phosphocholines were at significantly lower levels in peripheral tissue when compared to central tissue in both D5-1000 and D5-5000 mice (Figures 4E, 4F, and 5F). Fold differences and p-values for all mentioned metabolites can be found in Table S1.

The impact of infection in D20-1000 mice demonstrated different spatial patterns than in D5-1000 and D5-5000 mice. Amino acids and eicosanoids exhibited comparable impact of infection in peripheral and central segments (Table S1). Arachidonic acid did not demonstrate any substantial localized effects

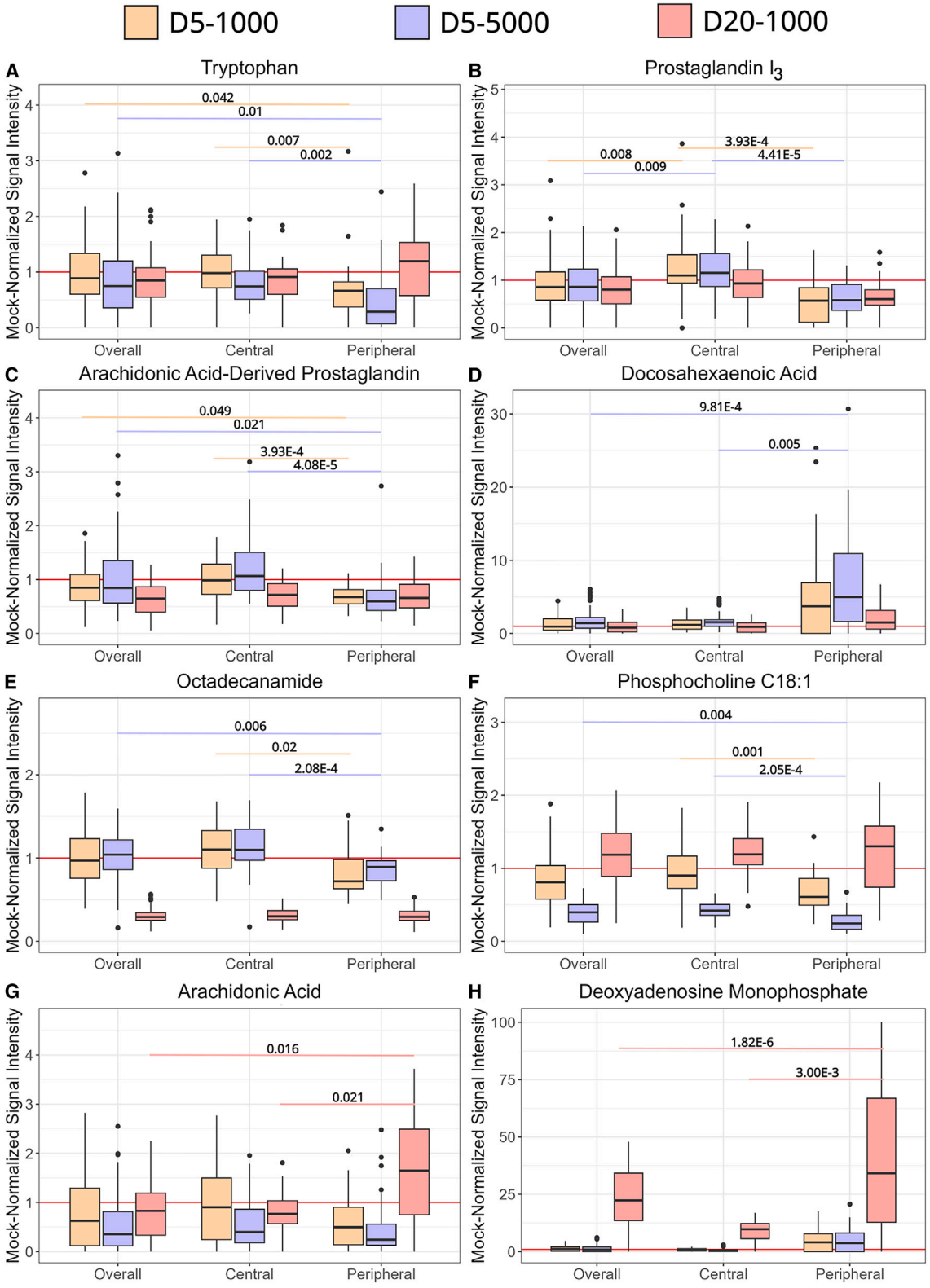

(legend on next page)

in D5-1000 or D5-5000 mice; however, the impact of infection on arachidonic acid was two times higher in peripheral levels than central levels in D20-1000 mice (Figure 5G). Deoxyadenosine monophosphate (Figure 5H) was over 3 times higher in peripheral lung tissue than central lung tissue in D20-1000.

Peripheral and central lung tissue shows innate differences in metabolite distribution prior to severe acute respiratory syndrome coronavirus 2 infection

Since the SARS-CoV-2 virus demonstrated preferential localization to central lung tissue while infection was associated with higher levels of metabolic perturbance in the peripheral lung tissue, we sought to understand factors that could contribute to viral and metabolic localization. When analyzing the periphery of the mock-infected lungs, mice innately had higher levels of fatty amides while having lower levels of amino acids, acylcarnitines, phosphocholines, glycerolipids, and eicosanoids (Figure 6A). Fatty acids were also significantly altered but presented with mixed directions of change in the periphery.

Tryptophan (Figure 6B), tyrosine, phenylalanine, and methionine were all significantly lower in peripheral tissue when compared to central tissue (Table S1). While both arachidonic acid (Figure 6C) and docosahexaenoic acid were significantly lower in the peripheral lung tissue, eicosapentaenoic acid was not significantly different between central and peripheral lung tissue. Of the previously discussed eicosanoids, only $PGF_{2\alpha}$ showed any spatial segregation, with central segments showing higher levels relative to peripheral segments (Figure 6D). With the exception of acetylcarnitine, acylcarnitines tended to be lower in the peripheral tissue (Table S1). Myristoylcarnitine (Figure 6F) and hexanoylcarnitine were both significantly lower while carnitine (Figure 6E) and oleoylcarnitine were not significantly different between the lung segments. Guanine, guanosine, and xanthine (Figure 6G) were all significantly lower in peripheral tissue, but urate (Figure 6H) did not show any significant differences.

DISCUSSION

Currently, metabolomics studies of COVID-19 have focused on the analysis of biofluids (plasma, serum, and so forth), but biofluids cannot fully encapsulate the intricacies of metabolism in the lungs. Indeed, analysis of lung tissue in other infection systems has revealed new findings not observed through biofluids or that contradict those found in a biofluid.[42,43] To address this gap, we systematically analyzed lung samples from a mouse model of SARS-CoV-2 infection, using the mouse-adapted SARS2-N501Y_{MA30} virus.[28] In this study, infection at two different viral doses and two different time points demonstrated a depleting effect on metabolism, with the majority of metabolites showing a decrease compared to mock-infected samples (Figures 1F–1H). This stands in contrast to findings in plasma and serum, where acylcarnitines,[21,44,45] the amino acids phenylalanine and methionine,[46–48] and purines[49,50] were all elevated with COVID-19.

COVID-19 unevenly impacts the lower respiratory system, particularly the lower lobes of the lungs.[13,14] A strength of spatial metabolomics (“chemical cartography”) studies is the ability to define how different regions of a given tissue respond to infection.[51] The implementation of this approach in this study demonstrated localized effects of SARS-CoV-2 infection in central and peripheral lung tissue, with the strongest metabolic impact observed in the lower left lung (Figure 3). Post-infection viral load tended to be highest in central lung tissue, while metabolic disturbance was highest in peripheral tissue. Fatty acids, amino acids, and eicosanoids were all more strongly decreased by infection in the peripheral D5-1000 and D5-5000 lung tissue than in central lung tissue. These localized effects of metabolism could help explain why peripheral lung tissue tends to be impacted more by COVID-19.

It is well known that amino acids show signs of dysregulation in biofluids from patients with COVID-19 and other viral conditions.[52–54] We observed this trend of amino acid dysregulation in the lungs overall (Figures 2A–2D), with the majority of significantly altered amino acids showing decreases upon infection, but we also discovered spatial trends in amino acid distribution. Mock-infected mice exhibited higher levels of amino acids in the central portions of the lung when compared to the peripheral portion (Figures 6A and 6B). In infected mice, amino acids were more strongly decreased by infection in the peripheral lung when compared to the central lung (Figures 4E–4G and 5A). Higher availability of amino acids in the central lung could make it easier for SARS-CoV-2 to replicate, leading to higher viral loads in these portions of the lung. Increases to the ratio of kynurenine to tryptophan have been associated with the severity of COVID-19.[55,56] The significant decrease in tryptophan and a significant increase in kynurenine associated only with D5-5000 mice corresponds well with the 5000 pfu dosage being lethal and the 1000 pfu dosage being survivable (Figure 2D; Figure S4). Glutamine, glutamate, and aspartate all correlated with viral load across D5-1000 and D5-5000 mice combined (spearman rho = 0.34, 0.44, and 0.53, respectively). These three amino acids are all part of glutamine metabolism, which is increased in immune cells such as macrophages and lymphocytes.[57,58] The correlation between glutamine metabolites and regions rich with viral load could be a result of

Figure 5. SARS-CoV-2 infection has localized effects on individual metabolites

(Mock-infected groups - n = 5 mice; 59 lung sections. Infected groups - n = 6 mice; D5-1000 = 69 lung sections, D5-5000 = 72 sections, D20-1000 = 71 sections). (A–H) Boxplots comparing impact of infection on overall, central, and peripheral levels of (A) tryptophan, (B) prostaglandin I_3, (C) an unannotated arachidonic acid-derived prostaglandin (m/z 353.23), (D) docosahexaenoic acid, (E) octadecanamide, (F) phosphocholine C18:1, (G) arachidonic acid, and (H) deoxyadenosine monophosphate in D5-1000 (orange), D5-5000 (purple), and D20-1000 mice (red). All metabolite signal intensities were normalized to the median signal intensity of the mock-infected mice for each position. P-values were calculated for intergroup comparisons for each disease state using the Wilcoxon test and were adjusted using the Bonferroni method. Only significant p-values are shown. The red line represents a fold difference of 1. The upper hinge represents the 75th percentile, the middle line represents the 50th percentile, and the lower hinge represents the 25th percentile. Each whisker extends from its respective hinge by 1.5 times the interquartile range of the hinge. Also, see Table S1.

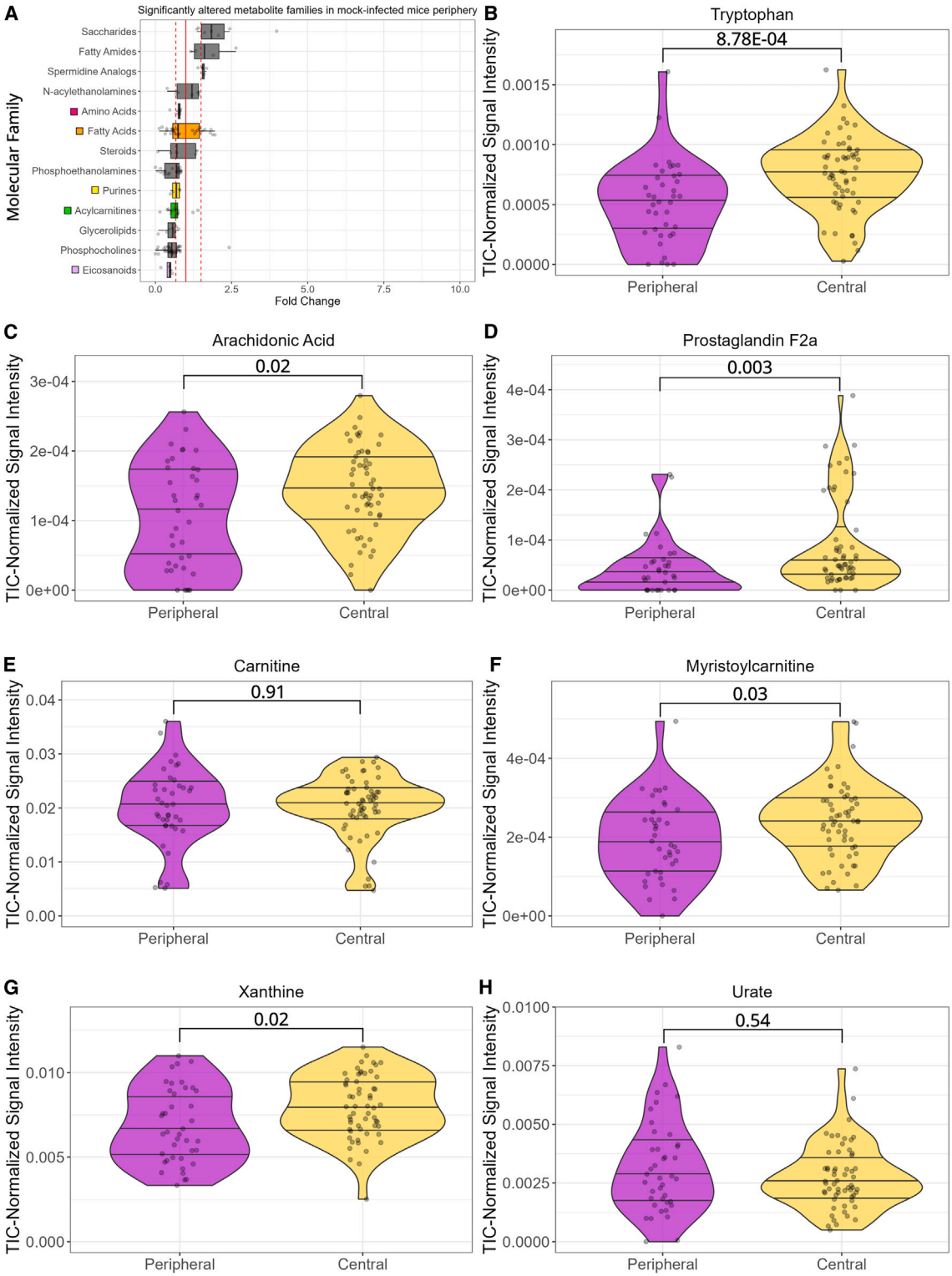

Figure 6. Peripheral and central lung tissue shows innate differences in metabolite distribution prior to SARS-CoV-2 infection

(Mock-infected groups - *n* = 5 mice; 59 lung sections. Infected groups - *n* = 6 mice; D5-1000 = 69 lung sections, D5-5000 = 72 sections, D20-1000 = 71 sections). (A) Significantly altered molecular families between central mock-infected lung tissue and peripheral mock-infected lung tissue. Fold changes are the median value of the metabolite in the peripheral tissue divided by the median value of the metabolite in the central tissue. All families depicted had at least 4 annotated

(legend continued on next page)

the recruitment of immune cells to fight off viral infection and proliferation.

Prostaglandin D_2 and prostaglandin $F_{2\alpha}$ have a complicated role in immune response regulation across the body, with a mixture of both pro-inflammatory and anti-inflammatory responses.[28,33,59–63] PGD_2 and $PGF_{2\alpha}$ were not significantly altered overall in D5-1000 mice and D20-1000 mice, but significantly higher in D5-5000 mice (Figure 2F); arachidonic acid, the precursor to PGD_2 and $PGF_{2\alpha}$, was significantly lower in D5-5000 mice, which has been observed in other studies of COVID-19 (Figure 2E).[64] In murine SARS-CoV-2 infection, PGD_2 signaling had deleterious effects on animal survival, viral clearance, and lung edema.[28] PGD_2 increases in the lungs as a natural result of aging, amplifying the increase of PGD_2 displayed with increased disease severity and potentially serving as one of the factors for increased mortality in elderly patients.[28] On the other hand, prostaglandin I_3, an anti-inflammatory eicosanoid and key mediator in inflammatory responses,[65] was not significantly altered overall. Despite this, PGI_3 levels were significantly lower in D5-1000 and D5-5000 peripheral lung tissue when compared to central lung tissue (Figure 5B). While not directly related to anti-inflammatory eicosanoid production, docosahexaenoic acid (DHA) was significantly higher in the peripheral tissue of D5-5000 mice (Figure 5D). DHA serves as a precursor for anti-inflammatory protectins and resolvins,[66] so higher levels of free DHA could be a result of the decreased production of these anti-inflammatory products. A healthy inflammatory response requires a balanced mixture of ω-3 and ω-6 derived eicosanoids, protectins, and resolvins.[67] In D5-5000, we see a clear preponderance of disease-promoting and pro-inflammatory metabolites in the overall lung without an equal response in anti-inflammatory metabolites. The use of ω-3 fatty acid supplements of DHA and EPA has been proposed as a method for combating severe COVID-19[66,68,69] but double-blind clinical studies investigating this treatment method either do not have publicly available results or have been terminated due to difficulty with patient enrollment.[70–72]

Infected mice had significantly lower levels of purine nucleosides. Viruses are known to upregulate metabolites necessary for their replication such as nucleotides and amino acids. Here, we see a pattern of depletion in these groups, possibly indicating incorporation into viral macromolecules, leading to lower levels of free nucleotides and amino acids detectable by metabolomics analysis. In D5-5000 mice, the end product of purine metabolism, urate, was significantly increased. Cell death leads to the increased production of urate, which in turn causes a pro-inflammatory response.[73–75] Additionally, the production of urate from purines causes the release of radical oxidative species, which can cause oxidative stress.[76] Gout, an inflammatory joint condition marked by increased levels of urate, has been linked to an increased likelihood of COVID-19 and COVID-19 disease severity.[77–79] While this has been theorized to be a result of comorbidities, here we see that severe COVID-19 disease results in elevated urate levels in the lungs, which could compound upon existing hyperuricemia and lead to worse patient outcomes. Colchicine, an anti-inflammatory drug sometimes prescribed to gout patients, has shown some success in reducing the severity of COVID-19 in patients with PCR-confirmed cases,[80] but urate-lowering therapy did not reduce COVID-19 severity.[78,81] The greater efficacy of generalized anti-inflammatory treatments compared to treatments focused purely on urate reduction is consistent with the fact that the increased levels of urate are just one of the several pro-inflammatory metabolite changes in SARS-CoV-2 infected mice.

Weight shows a strong negative correlation with viral load across the three infection states (rho = −0.602, p-value = 2.68E-22). To identify if metabolites significantly altered in this model could be driven by weight loss associated with acute SARS-CoV-2 infection, we compared our results with data previously generated in mice infected with the influenza virus, where weight loss is also observed in the acute stage.[10] Less than 10% of impacted metabolites in each infection group were also significant in the influenza model, meaning that the majority of perturbed metabolites likely were not driven by weight loss alone (Figure S7). Included in this overlap were glutamine, EpETE, DHA, Prostaglandin I_3, carnitine, propionylcarnitine, hydroxybutyrylcarnitine, and urate. These metabolites could either be a result of weight loss or could be generally perturbed by viral infections in the lungs. Additionally, D20-1000 mice had returned to their original weight by experimental endpoint but still presented with comparable viral load to D5-1000 mice (Figure 3; Figure S8) and with significant metabolomic alterations that largely overlapped with the D5 mice (Figure 1C). Over half of the metabolites significantly altered in D5-1000 and D5-5000 were significantly altered in D20-1000, including key amino acids, fatty acids, and acylcarnitines (Figure 1C). Jointly, these observations suggest that while weight loss likely plays a role in the metabolic effects of SARS-CoV-2 infection, other causal factors are also involved, such as direct metabolite consumption as viral building blocks or ongoing immune effects on metabolism.

The primary difference between D20-1000 and D5-1000 mice appeared to be in purine metabolism. Guanosine monophosphate was detected in D5-1000 and D5-5000 mice, but not in D20-1000 mice, indicating lowered levels. In addition to lower guanosine monophosphate, D20-1000 had significant increases in guanine and guanosine not present in D5-1000 mice, suggesting decreased usage of the purine salvage pathway. This could be a result of decreased viral replication at this stage of infection, which would decrease the need for GMP/AMP and therefore increase free purines, or it could be an overcompensation in response to the purine depletion seen in D5-1000 mice.

metabolites belonging to that family. Dashed red lines represent a fold change of 0.67 or 1.5 while the solid red line represents a fold change of 1. Family colors as in Figure 2. Data represented as median fold change. The upper hinge represents the 75th percentile, the middle line represents the 50th percentile, and the lower hinge represents the 25th percentile. Each whisker extends from its respective hinge by 1.5 times the interquartile range of the hinge.

(B–H) Violin plots of individual metabolites of interest. Each dot represents the signal intensity of that metabolite in one lung segment. P-values were calculated for intergroup comparisons for each disease state using the Wilcoxon test and were adjusted using the false discovery rate method. From top to bottom, each line represents the 100th, 75th, 50th, 25th, and 0th percentile, respectively. Also, see Table S1.

In spite of the strong genetic similarity of inbred C57BL/6J mice, D20-1000 mice presented with a range of recovery responses, with some mice showing overall metabolic recovery, and others showing persistently perturbed metabolism (Figure S2A). Lung recovery also varied based on lung segment; upper lung segments of D20-1000 mice had similar metabolic profiles to upper lung segments of D5-1000 mice, while lower lung segments displayed significant metabolic differences that trended toward metabolic recovery, suggesting uneven healing in the lungs as the viral load resolves (Figure S2B; Table S4). Jointly, these results may represent a path toward understanding the heterogeneity in long COVID development, though studies of later time points will be necessary. Future studies of COVID-19 recovery and long COVID should also investigate the metabolism of the brain, pancreas, and heart, based on symptoms seen during acute and post-acute COVID-19.

To our knowledge, this is the first study that performed spatial metabolomics analysis on SARS-CoV-2 infected lungs. We observed higher viral loads in central lung tissue. In spite of this, metabolic changes were largest in peripheral lung tissue, matching the higher levels of peripheral lung tissue damage observed in humans. Mock-infected mice had innately higher levels of acylcarnitines, amino acids, fatty acids, and purines in their central lung tissue, which might aid in SARS-CoV-2's localization to centralized lung tissue. Infected lung tissue presented with significantly lower levels of acylcarnitines, fatty acids, and amino acids. Several fatty acids and amino acids demonstrated significantly different levels of metabolites in peripheral lung tissue, where the largest degree of lung damage is observed in humans. These findings, which were only achieved due to spatial analysis of lung tissue, help contextualize localized effects of COVID-19 in the lungs and provide insight on potential molecular families to target for the future mitigation of COVID-19 symptoms.

Limitations of the study

This study used the mouse-adapted SARS-CoV-2 strain SARS2-N501Y$_{MA30}$ for infection in wild-type mice. While this strain of SARS-CoV-2 provides a good experimental model for COVID-19 infection,[28] it is neither the same strain of SARS-CoV-2 that infects humans, nor the latest strain of SARS-CoV-2 since the virus mutates rapidly.[82] The mice used in this study were exclusively female, matching prior spatial metabolomics analyses we have performed with influenza and minimizing the need to rehouse or singly house fighting male mice. Sex-matched mock-infected groups control for sex-specific metabolites not related to the effects of infection. However, mice can still show sex-specific effects in response to infection.[8,83,84] Nevertheless, we observed many similarities between the chemical classes that are significantly altered in human studies and in our data.[85–87] Additionally, the localized effects in peripheral lung tissue observed in this model match those seen in humans.[14,16–18] Metabolomic differences between human data and this study may be due to the use of a mouse model, or to the fact that most human studies were restricted to biofluids, whereas our mouse model enabled the analysis of lung tissue, the primary site of infection for SARS-CoV-2. Future studies should investigate peripheral lung metabolism in the transverse plane, as this region frequently shows ground-glass opacities on X-ray and CT scans.[88]

RESOURCE AVAILABILITY

Lead contact

Further information and requests for resources should be directed to and will be fulfilled by the lead contact, Dr. Laura-Isobel McCall (lmccall@sdsu.edu).

Material availability

This study did not generate new unique reagents.

Data and code availability

- Data: Raw data files have been deposited into MassIVE: MSV000094591 (https://doi.org/10.25345/C51Z42451) and are publicly available at the time of publication. The final GNPS feature-based molecular network job can be accessed through the following URL: https://gnps.ucsd.edu/ProteoSAFe/status.jsp?task=0950a8281f6748e783e419ae5bdf6d85.
- Code: An R markdown notebook of code used for the project can be found at https://github.com/jarrodRoachChem/covid19.
- All other requests: Any additional information required to reanalyze the data reported in this article is available from the lead contact upon request.

ACKNOWLEDGMENTS

This project was supported by start-up funds to L-I.M and by funds from the National Institutes of Health (P01 AI060699 and R01 AI129269) to SP. L-I.M. holds an Investigators in the Pathogenesis of Infectious Disease Award from the Burroughs Wellcome Fund.

AUTHOR CONTRIBUTIONS

Conceptualization, L-I.M.; methodology, J.L., S.P., and L-I.M.; software, J.L.; formal analysis, J.L.; investigation, J.L., B.X., J.Z., and M.N.; resources, S.P. and L-I.M.; data curation, J.L.; writing – original draft, J.L.; writing – review and editing, J.L., B.X., J.Z., M.N., S.P., and L-I.M.; visualization, J.L.; supervision, L-I.M.; project administration, L-I.M.; funding acquisition, S.P. and L-I.M.

DECLARATION OF INTERESTS

The authors declare no competing interests.

STAR★METHODS

Detailed methods are provided in the online version of this paper and include the following:

- KEY RESOURCES TABLE
- EXPERIMENTAL MODEL AND STUDY PARTICIPANT DETAILS
  - SARS-CoV-2 model
  - Mouse infection
- METHOD DETAILS
  - Metabolite extraction
  - LC-MS/MS data collection
- QUANTIFICATION AND STATISTICAL ANALYSIS
  - Viral load analysis
  - Raw data processing
  - Data analysis
  - Statistical analysis

SUPPLEMENTAL INFORMATION

Supplemental information can be found online at https://doi.org/10.1016/j.isci.2024.111727.

Received: June 17, 2024
Revised: October 30, 2024
Accepted: December 30, 2024
Published: January 2, 2025

REFERENCES

1. COVID-19 deaths. datadot. https://data.who.int/dashboards/covid19/deaths?n=c.
2. Hillary, V.E., and Ceasar, S.A. (2023). An Update on COVID-19: SARS-CoV-2 Variants, Antiviral Drugs, and Vaccines. Heliyon *9*, e13952.
3. Altmann, D.M., Whettlock, E.M., Liu, S., Arachchillage, D.J., and Boyton, R.J. (2023). The Immunology of Long COVID. Nat. Rev. Immunol. *23*, 618–634.
4. Ballering, A.V., van Zon, S.K.R., Olde Hartman, T.C., and Rosmalen, J.G.M.; Lifelines Corona Research Initiative (2022). Persistence of Somatic Symptoms after COVID-19 in the Netherlands: An Observational Cohort Study. Lancet *400*, 452–461.
5. Davis, H.E., McCorkell, L., Vogel, J.M., and Topol, E.J. (2023). Long COVID: Major Findings, Mechanisms and Recommendations. Nat. Rev. Microbiol. *21*, 133–146.
6. Wishart, D.S. (2019). Metabolomics for Investigating Physiological and Pathophysiological Processes. Physiol. Rev. *99*, 1819–1875.
7. Lorente, J.A., Nin, N., Villa, P., Vasco, D., Miguel-Coello, A.B., Rodriguez, I., Herrero, R., Peñuelas, O., Ruiz-Cabello, J., and Izquierdo-Garcia, J.L. (2021). Metabolomic Diferences between COVID-19 and H1N1 Influenza Induced ARDS. Crit. Care *25*, 390.
8. Dean, D.A., Roach, J., Ulrich vonBargen, R., Xiong, Y., Kane, S.S., Klechka, L., Wheeler, K., Jimenez Sandoval, M., Lesani, M., Hossain, E., et al. (2023). Persistent Biofluid Small-Molecule Alterations Induced by Trypanosoma Cruzi Infection Are Not Restored by Parasite Elimination. ACS Infect. Dis. *9*, 2173–2189.
9. Dean, D.A., Gautham, G., Siqueira-Neto, J.L., McKerrow, J.H., Dorrestein, P.C., and McCall, L.-I. (2021). Spatial Metabolomics Identifies Localized Chemical Changes in Heart Tissue during Chronic Cardiac Chagas Disease. PLoS Negl. Trop. Dis. *15*, e0009819.
10. Dean, D.A., Klechka, L., Hossain, E., Parab, A.R., Eaton, K., Hinsdale, M., and McCall, L.-I. (2022). Spatial Metabolomics Reveals Localized Impact of Influenza Virus Infection on the Lung Tissue Metabolome. mSystems *7*, e0035322.
11. Stopka, S.A., van der Reest, J., Abdelmoula, W.M., Ruiz, D.F., Joshi, S., Ringel, A.E., Haigis, M.C., and Agar, N.Y.R. (2022). Spatially Resolved Characterization of Tissue Metabolic Compartments in Fasted and High-Fat Diet Livers. PLoS One *17*, e0261803.
12. Liu, Z., Ulrich vonBargen, R., Kendricks, A.L., Wheeler, K., Leão, A.C., Sankaranarayanan, K., Dean, D.A., Kane, S.S., Hossain, E., Pollet, J., et al. (2023). Localized Cardiac Small Molecule Trajectories and Persistent Chemical Sequelae in Experimental Chagas Disease. Nat. Commun. *14*, 6769.
13. Kalafat, E., Yaprak, E., Cinar, G., Varli, B., Ozisik, S., Uzun, C., Azap, A., and Koc, A. (2020). Lung Ultrasound and Computed Tomographic Findings in Pregnant Woman with COVID-19. Ultrasound Obstet. Gynecol. *55*, 835–837.
14. Bernheim, A., Mei, X., Huang, M., Yang, Y., Fayad, Z.A., Zhang, N., Diao, K., Lin, B., Zhu, X., Li, K., et al. (2020). Chest CT Findings in Coronavirus Disease-19 (COVID-19): Relationship to Duration of Infection. Radiology *295*, 200463.
15. Rousan, L.A., Elobeid, E., Karrar, M., and Khader, Y. (2020). Chest X-Ray Findings and Temporal Lung Changes in Patients with COVID-19 Pneumonia. BMC Pulm. Med. *20*, 245.
16. Meng, H., Xiong, R., He, R., Lin, W., Hao, B., Zhang, L., Lu, Z., Shen, X., Fan, T., Jiang, W., et al. (2020). CT Imaging and Clinical Course of Asymptomatic Cases with COVID-19 Pneumonia at Admission in Wuhan, China. J. Infect. *81*, e33–e39.
17. Wu, J., Wu, X., Zeng, W., Guo, D., Fang, Z., Chen, L., Huang, H., and Li, C. (2020). Chest CT Findings in Patients With Coronavirus Disease 2019 and Its Relationship With Clinical Features. Invest. Radiol. *55*, 257–261.
18. Adams, H.J.A., Kwee, T.C., Yakar, D., Hope, M.D., and Kwee, R.M. (2020). Chest CT Imaging Signature of Coronavirus Disease 2019 Infection: In Pursuit of the Scientific Evidence. Chest *158*, 1885–1895.
19. Yang, K., Kang, Z., Guan, W., Lotfi-Emran, S., Mayer, Z.J., Guerrero, C.R., Steffen, B.T., Puskarich, M.A., Tignanelli, C.J., Lusczek, E., and Safo, S.E. (2023). Developing A Baseline Metabolomic Signature Associated with COVID-19 Severity: Insights from Prospective Trials Encompassing 13 U.S. Centers. Metabolites *13*, 1107. https://doi.org/10.3390/metabo13111107.
20. Gygi, J.P., Maguire, C., Patel, R.K., Shinde, P., Konstorum, A., Shannon, C.P., Xu, L., Hoch, A., Jayavelu, N.D., Network, I., et al. (2023). Integrated Longitudinal Multi-Omics Study Identifies Immune Programs Associated with COVID-19 Severity and Mortality in 1152 Hospitalized Participants. Preprint at bioRxiv. https://doi.org/10.1101/2023.11.03.565292.
21. Valdés, A., Moreno, L.O., Rello, S.R., Orduña, A., Bernardo, D., and Cifuentes, A. (2022). Metabolomics Study of COVID-19 Patients in Four Different Clinical Stages. Sci. Rep. *12*, 1650.
22. Kimhofer, T., Lodge, S., Whiley, L., Gray, N., Loo, R.L., Lawler, N.G., Nitschke, P., Bong, S.-H., Morrison, D.L., Begum, S., et al. (2020). Integrative Modeling of Quantitative Plasma Lipoprotein, Metabolic, and Amino Acid Data Reveals a Multiorgan Pathological Signature of SARS-CoV-2 Infection. J. Proteome Res. *19*, 4442–4454.
23. López-Hernández, Y., Monárrez-Espino, J., López, D.A.G., Zheng, J., Borrego, J.C., Torres-Calzada, C., Elizalde-Díaz, J.P., Mandal, R., Berjanskii, M., Martínez-Martínez, E., et al. (2023). The Plasma Metabolome of Long COVID Patients Two Years after Infection. Sci. Rep. *13*, 12420.
24. Soares, N.C., Hussein, A., Muhammad, J.S., Semreen, M.H., ElGhazali, G., and Hamad, M. (2023). Plasma Metabolomics Profiling Identifies New Predictive Biomarkers for Disease Severity in COVID-19 Patients. PLoS One *18*, e0289738.
25. Roberts, I., Wright Muelas, M., Taylor, J.M., Davison, A.S., Xu, Y., Grixti, J.M., Gotts, N., Sorokin, A., Goodacre, R., and Kell, D.B. (2021). Untargeted Metabolomics of COVID-19 Patient Serum Reveals Potential Prognostic Markers of Both Severity and Outcome. Metabolomics *18*, 6.
26. Liu, J., Li, Z.-B., Lu, Q.-Q., Yu, Y., Zhang, S.-Q., Ke, P.-F., Zhang, F., and Li, J.-C. (2022). Metabolite Profile of COVID-19 Revealed by UPLC-MS/MS-Based Widely Targeted Metabolomics. Front. Immunol. *13*, 894170.
27. Bi, X., Liu, W., Ding, X., Liang, S., Zheng, Y., Zhu, X., Quan, S., Yi, X., Xiang, N., Du, J., et al. (2022). Proteomic and Metabolomic Profiling of Urine Uncovers Immune Responses in Patients with COVID-19. Cell Rep. *38*, 110271.
28. Wong, L.-Y.R., Zheng, J., Wilhelmsen, K., Li, K., Ortiz, M.E., Schnicker, N.J., Thurman, A., Pezzulo, A.A., Szachowicz, P.J., Li, P., et al. (2022). Eicosanoid Signalling Blockade Protects Middle-Aged Mice from Severe COVID-19. Nature *605*, 146–151.
29. Baumgartner, R., Forteza, M.J., and Ketelhuth, D.F. (2019). The Interplay between Cytokines and the Kynurenine Pathway in Inflammation and Atherosclerosis. Cytokine *122*, 154148.
30. Calder, P.C. (2010). Omega-3 Fatty Acids and Inflammatory Processes. Nutrients *2*, 355–374.
31. Pal, A., Metherel, A.H., Fiabane, L., Buddenbaum, N., Bazinet, R.P., and Shaikh, S.R. (2020). Do Eicosapentaenoic Acid and Docosahexaenoic Acid Have the Potential to Compete against Each Other? Nutrients *12*, 3718. https://doi.org/10.3390/nu12123718.
32. Calder, P.C. (2017). Omega-3 Fatty Acids and Inflammatory Processes: From Molecules to Man. Biochem. Soc. Trans. *45*, 1105–1115.
33. Domingo, C., Palomares, O., Sandham, D.A., Erpenbeck, V.J., and Altman, P. (2018). The Prostaglandin D2 Receptor 2 Pathway in Asthma: A Key Player in Airway Inflammation. Respir. Res. *19*, 189.

34. Murray, J.J., Tonnel, A.B., Brash, A.R., Roberts, L.J., 2nd, Gosset, P., Workman, R., Capron, A., and Oates, J.A. (1986). Release of Prostaglandin D2 into Human Airways during Acute Antigen Challenge. N. Engl. J. Med. *315*, 800–804.

35. Hardy, C.C., Robinson, C., Tattersfield, A.E., and Holgate, S.T. (1984). The Bronchoconstrictor Effect of Inhaled Prostaglandin D2 in Normal and Asthmatic Men. N. Engl. J. Med. *311*, 209–213.

36. Mathé, A.A., Hedqvist, P., Holmgren, A., and Svanborg, N. (1973). Bronchial Hyperreactivity to Prostaglandin F 2 and Histamine in Patients with Asthma. Br. Med. J. *1*, 193–196.

37. Le, H.D., Meisel, J.A., de Meijer, V.E., Gura, K.M., and Puder, M. (2009). The Essentiality of Arachidonic Acid and Docosahexaenoic Acid. Prostaglandins Leukot. Essent. Fatty Acids *81*, 165–170.

38. Lands, W.E. (1992). Biochemistry and Physiology of N-3 Fatty Acids. FASEB J. *6*, 2530–2536.

39. Cui, J., Shan, K., Yang, Q., Qi, Y., Qu, H., Li, J., Wang, R., Jia, L., Chen, W., Feng, N., and Chen, Y.Q. (2021). Prostaglandin E3 Attenuates Macrophage-Associated Inflammation and Prostate Tumour Growth by Modulating Polarization. J. Cell Mol. Med. *25*, 5586–5601.

40. Araujo, P., Espe, M., Lucena, E., Yang, Y., and Holen, E. (2021). Differential Production of Prostaglandins and Prostacyclins by Liver and Head Kidney Cells from Atlantic Salmon Challenged with Arachidonic and Eicosapentaenoic Acids. Fish Shellfish Immunol. Rep. *2*, 100015.

41. (2016). Carnitine Transport and Fatty Acid Oxidation. Biochim. Biophys. Acta Mol. Cell Res. *1863*, 2422–2435.

42. Bernatchez, J.A., and McCall, L.-I. (2020). Insights Gained into Respiratory Infection Pathogenesis Using Lung Tissue Metabolomics. PLoS Pathog. *16*, e1008662.

43. Saoi, M., and Britz-McKibbin, P. (2021). New Advances in Tissue Metabolomics: A Review. Metabolites *11*, 672. https://doi.org/10.3390/metabo11100672.

44. Martínez-Gómez, L.E., Ibarra-González, I., Fernández-Lainez, C., Tusie, T., Moreno-Macías, H., Martinez-Armenta, C., Jimenez-Gutierrez, G.E., Vázquez-Cárdenas, P., Vidal-Vázquez, P., Ramírez-Hinojosa, J.P., et al. (2022). Metabolic Reprogramming in SARS-CoV-2 Infection Impacts the Outcome of COVID-19 Patients. Front. Immunol. *13*, 936106.

45. Herrera-Van Oostdam, A.S., Castañeda-Delgado, J.E., Oropeza-Valdez, J.J., Borrego, J.C., Monárrez-Espino, J., Zheng, J., Mandal, R., Zhang, L., Soto-Guzmán, E., Fernández-Ruiz, J.C., et al. (2021). Immunometabolic Signatures Predict Risk of Progression to Sepsis in COVID-19. PLoS One *16*, e0256784.

46. Maltais-Payette, I., Lajeunesse-Trempe, F., Pibarot, P., Biertho, L., and Tchernof, A. (2023). Association between Circulating Amino Acids and COVID-19 Severity. Metabolites *13*, 201.

47. Danlos, F.-X., Grajeda-Iglesias, C., Durand, S., Sauvat, A., Roumier, M., Cantin, D., Colomba, E., Rohmer, J., Pommeret, F., Baciarello, G., et al. (2021). Metabolomic Analyses of COVID-19 Patients Unravel Stage-Dependent and Prognostic Biomarkers. Cell Death Dis. *12*, 258.

48. Gardinassi, L.G., Servian, C.d.P., Lima, G.d.S., Dos Anjos, D.C.C., Gomes Junior, A.R., Guilarde, A.O., Borges, M.A.S.B., Dos Santos, G.F., Moraes, B.G.N., Silva, J.M.M., et al. (2023). Integrated Metabolic and Inflammatory Signatures Associated with Severity Of, Fatality Of, and Recovery from COVID-19. Microbiol. Spectr. *11*, e0219422.

49. Caterino, M., Costanzo, M., Fedele, R., Cevenini, A., Gelzo, M., Di Minno, A., Andolfo, I., Capasso, M., Russo, R., Annunziata, A., et al. (2021). The Serum Metabolome of Moderate and Severe COVID-19 Patients Reflects Possible Liver Alterations Involving Carbon and Nitrogen Metabolism. Int. J. Mol. Sci. *22*, 9548. https://doi.org/10.3390/ijms22179548.

50. Doğan, H.O., Şenol, O., Bolat, S., Yıldız, Ş.N., Büyüktuna, S.A., Sarıismailoğlu, R., Doğan, K., Hasbek, M., and Hekim, S.N. (2021). Understanding the Pathophysiological Changes via Untargeted Metabolomics in COVID-19 Patients. J. Med. Virol. *93*, 2340–2349.

51. McCall, L.-I., Morton, J.T., Bernatchez, J.A., de Siqueira-Neto, J.L., Knight, R., Dorrestein, P.C., and McKerrow, J.H. (2017). Mass Spectrometry-Based Chemical Cartography of a Cardiac Parasitic Infection. Anal. Chem. *89*, 10414–10421.

52. Tomé, D. (2021). Amino Acid Metabolism and Signalling Pathways: Potential Targets in the Control of Infection and Immunity. Eur. J. Clin. Nutr. *75*, 1319–1327.

53. Masoodi, M., Peschka, M., Schmiedel, S., Haddad, M., Frye, M., Maas, C., Lohse, A., Huber, S., Kirchhof, P., Nofer, J.-R., and Renné, T. (2022). Disturbed Lipid and Amino Acid Metabolisms in COVID-19 Patients. J. Mol. Med. *100*, 555–568.

54. Shen, B., Yi, X., Sun, Y., Bi, X., Du, J., Zhang, C., Quan, S., Zhang, F., Sun, R., Qian, L., et al. (2020). Proteomic and Metabolomic Characterization of COVID-19 Patient Sera. Cell *182*, 59–72.e15.

55. Dewulf, J.P., Martin, M., Marie, S., Oguz, F., Belkhir, L., De Greef, J., Yombi, J.C., Wittebole, X., Laterre, P.-F., Jadoul, M., et al. (2022). Urine Metabolomics Links Dysregulation of the Tryptophan-Kynurenine Pathway to Inflammation and Severity of COVID-19. Sci. Rep. *12*, 9959.

56. Lionetto, L., Ulivieri, M., Capi, M., De Bernardini, D., Fazio, F., Petrucca, A., Pomes, L.M., De Luca, O., Gentile, G., Casolla, B., et al. (2021). Increased Kynurenine-to-Tryptophan Ratio in the Serum of Patients Infected with SARS-CoV2: An Observational Cohort Study. Biochim. Biophys. Acta, Mol. Basis Dis. *1867*, 166042.

57. Ma, G., Zhang, Z., Li, P., Zhang, Z., Zeng, M., Liang, Z., Li, D., Wang, L., Chen, Y., Liang, Y., and Niu, H. (2022). Reprogramming of Glutamine Metabolism and Its Impact on Immune Response in the Tumor Microenvironment. Cell Commun. Signal. *20*, 114.

58. Field, C.J., Johnson, I., and Pratt, V.C. (2000). Glutamine and Arginine: Immunonutrients for Improved Health. Med. Sci. Sports Exerc. *32*, S377–S388.

59. Liu, M.C., Bleecker, E.R., Lichtenstein, L.M., Kagey-Sobotka, A., Niv, Y., McLemore, T.L., Permutt, S., Proud, D., and Hubbard, W.C. (1990). Evidence for Elevated Levels of Histamine, Prostaglandin D2, and Other Bronchoconstricting Prostaglandins in the Airways of Subjects with Mild Asthma. Am. Rev. Respir. Dis. *142*, 126–132.

60. Lee, K., Lee, S.H., and Kim, T.H. (2020). The Biology of Prostaglandins and Their Role as a Target for Allergic Airway Disease Therapy. Int. J. Mol. Sci. *21*, 1851. https://doi.org/10.3390/ijms21051851.

61. Ricciotti, E., and FitzGerald, G.A. (2011). Prostaglandins and Inflammation. Arterioscler. Thromb. Vasc. Biol. *31*, 986–1000.

62. Scher, J.U., and Pillinger, M.H. (2009). The Anti-Inflammatory Effects of Prostaglandins. J. Investig. Med. *57*, 703–708.

63. Wautier, J.-L., and Wautier, M.-P. (2023). Pro- and Anti-Inflammatory Prostaglandins and Cytokines in Humans: A Mini Review. Int. J. Mol. Sci. *24*, 9647. https://doi.org/10.3390/ijms24119647.

64. Castañé, H., Iftimie, S., Baiges-Gaya, G., Rodríguez-Tomàs, E., Jiménez-Franco, A., López-Azcona, A.F., Garrido, P., Castro, A., Camps, J., and Joven, J. (2022). Machine Learning and Semi-Targeted Lipidomics Identify Distinct Serum Lipid Signatures in Hospitalized COVID-19-Positive and COVID-19-Negative Patients. Metabolism *131*, 155197.

65. Tapiero, H., Ba, G.N., Couvreur, P., and Tew, K.D. (2002). Polyunsaturated Fatty Acids (PUFA) and Eicosanoids in Human Health and Pathologies. Biomed. Pharmacother. *56*, 215–222.

66. Lampova, B., Doskocil, I., Kourimska, L., and Kopec, A. (2022). N-3 Polyunsaturated Fatty Acids May Affect the Course of COVID-19. Front. Immunol. *13*, 957518.

67. Field, C.J., Johnson, I.R., and Schley, P.D. (2002). Nutrients and Their Role in Host Resistance to Infection. J. Leukoc. Biol. *71*, 16–32.

68. Weill, P., Plissonneau, C., Legrand, P., Rioux, V., and Thibault, R. (2020). May Omega-3 Fatty Acid Dietary Supplementation Help Reduce Severe Complications in Covid-19 Patients? Biochimie *179*, 275–280.

69. Harris, W.S., Tintle, N.L., Sathyanarayanan, S.P., and Westra, J. (2023). Association between Blood N-3 Fatty Acid Levels and the Risk of Coronavirus Disease 2019 in the UK Biobank. Am. J. Clin. Nutr. *117*, 357–363.

70. Feasibility Pilot Clinical Trial of Omega-3 Supplement vs. Placebo for Post Covid-19 Recovery Among Health Care Workers. https://classic.clinicaltrials.gov/ct2/show/study/NCT05121766.(accessed 2024-03-18)

71. ClinicalTrials.Gov. https://www.clinicaltrials.gov/study/NCT04647604?cond=Covid19&term=Fish%20Oils%20%7C%20omega-3&rank=2. (accessed 2024-03-18)

72. ClinicalTrials.Gov. https://www.clinicaltrials.gov/study/NCT04483271?cond=Covid19&term=Fish%20Oils%20%7C%20omega-3&rank=5&tab=results.(accessed 2024-03-18)

73. Kono, H., Chen, C.-J., Ontiveros, F., and Rock, K.L. (2010). Uric Acid Promotes an Acute Inflammatory Response to Sterile Cell Death in Mice. J. Clin. Invest. *120*, 1939–1949.

74. Shi, Y., Evans, J.E., and Rock, K.L. (2003). Molecular Identification of a Danger Signal That Alerts the Immune System to Dying Cells. Nature *425*, 516–521.

75. Ghaemi-Oskouie, F., and Shi, Y. (2011). The Role of Uric Acid as an Endogenous Danger Signal in Immunity and Inflammation. Curr. Rheumatol. Rep. *13*, 160–166.

76. Furuhashi, M. (2020). New Insights into Purine Metabolism in Metabolic Diseases: Role of Xanthine Oxidoreductase Activity. Am. J. Physiol. Endocrinol. Metab. *319*, E827–E834.

77. Jatuworapruk, K., Montgomery, A., Gianfrancesco, M., Conway, R., Durcan, L., Graef, E.R., Jayatilleke, A., Keen, H., Kilian, A., Young, K., et al. (2022). Characteristics and Outcomes of People With Gout Hospitalized Due to COVID-19: Data From the COVID-19 Global Rheumatology Alliance Physician-Reported Registry. ACR Open Rheumatol. *4*, 948–953.

78. Topless, R.K., Gaffo, A., Stamp, L.K., Robinson, P.C., Dalbeth, N., and Merriman, T.R. (2022). Gout and the Risk of COVID-19 Diagnosis and Death in the UK Biobank: A Population-Based Study. Lancet. Rheumatol. *4*, e274–e281.

79. Xie, D., Choi, H.K., Dalbeth, N., Wallace, Z.S., Sparks, J.A., Lu, N., Zeng, C., Li, X., Wei, J., Lei, G., and Zhang, Y. (2023). Gout and Excess Risk of Severe SARS-CoV-2 Infection Among Vaccinated Individuals: A General Population Study. Arthritis Rheumatol. *75*, 122–132.

80. Tardif, J.-C., Bouabdallaoui, N., L'Allier, P.L., Gaudet, D., Shah, B., Pillinger, M.H., Lopez-Sendon, J., da Luz, P., Verret, L., Audet, S., et al. (2021). Colchicine for Community-Treated Patients with COVID-19 (COLCORONA): A Phase 3, Randomised, Double-Blinded, Adaptive, Placebo-Controlled, Multicentre Trial. Lancet Respir. Med. *9*, 924–932.

81. Dufour, I., Werion, A., Belkhir, L., Wisniewska, A., Perrot, M., De Greef, J., Schmit, G., Yombi, J.C., Wittebole, X., Laterre, P.-F., et al. (2021). Serum Uric Acid, Disease Severity and Outcomes in COVID-19. Crit. Care *25*, 212.

82. Markov, P.V., Ghafari, M., Beer, M., Lythgoe, K., Simmonds, P., Stilianakis, N.I., and Katzourakis, A. (2023). The Evolution of SARS-CoV-2. Nat. Rev. Microbiol. *21*, 361–379.

83. Gay, L., Melenotte, C., Lakbar, I., Mezouar, S., Devaux, C., Raoult, D., Bendiane, M.-K., Leone, M., and Mège, J.-L. (2021). Sexual Dimorphism and Gender in Infectious Diseases. Front. Immunol. *12*, 698121.

84. Klein, S.L., and Flanagan, K.L. (2016). Sex Differences in Immune Responses. Nat. Rev. Immunol. *16*, 626–638.

85. Sindelar, M., Stancliffe, E., Schwaiger-Haber, M., Anbukumar, D.S., Adkins-Travis, K., Goss, C.W., O'Halloran, J.A., Mudd, P.A., Liu, W.-C., Albrecht, R.A., et al. (2021). Longitudinal Metabolomics of Human Plasma Reveals Prognostic Markers of COVID-19 Disease Severity. Cell Rep. Med. *2*, 100369.

86. Ansone, L., Briviba, M., Silamikelis, I., Terentjeva, A., Perkons, I., Birzniece, L., Rovite, V., Rozentale, B., Viksna, L., Kolesova, O., et al. (2021). Amino Acid Metabolism Is Significantly Altered at the Time of Admission in Hospital for Severe COVID-19 Patients: Findings from Longitudinal Targeted Metabolomics Analysis. Microbiol. Spectr. *9*, e0033821.

87. Archambault, A.-S., Zaid, Y., Rakotoarivelo, V., Turcotte, C., Doré, É., Dubuc, I., Martin, C., Flamand, O., Amar, Y., Cheikh, A., et al. (2021). High Levels of Eicosanoids and Docosanoids in the Lungs of Intubated COVID-19 Patients. Faseb. J. *35*, e21666.

88. Jacobi, A., Chung, M., Bernheim, A., and Eber, C. (2020). Portable Chest X-Ray in Coronavirus Disease-19 (COVID-19): A Pictorial Review. Clin. Imag. *64*, 35–42.

89. Ge, Q., Zhou, S., Porras, J., Fu, P., Wang, T., Du, J., and Li, K. (2024). SARS-CoV-2 Neurotropism-Induced Anxiety/depression-like Behaviors Require Microglia Activation. Preprint at bioRxiv, 2023.10.02.560570. https://doi.org/10.1101/2023.10.02.560570.

90. Verma, A.K., Zheng, J., Meyerholz, D.K., and Perlman, S. (2022). SARS-CoV-2 Infection of Sustentacular Cells Disrupts Olfactory Signaling Pathways. JCI insight *7*, e160277. https://doi.org/10.1172/jci.insight.160277.

91. Kibler, K.V., Szczerba, M., Lake, D., Roeder, A.J., Rahman, M., Hogue, B.G., Roy Wong, L.Y., Perlman, S., Li, Y., and Jacobs, B.L. (2022). Intranasal Immunization with a Vaccinia Virus Vaccine Vector Expressing Pre-Fusion Stabilized SARS-CoV-2 Spike Fully Protected Mice against Lethal Challenge with the Heavily Mutated Mouse-Adapted SARS2-N501YMA30 Strain of SARS-CoV-2. Vaccines *10*, 1172. https://doi.org/10.3390/vaccines10081172.

92. El-Kafrawy, S.A., Odle, A., Abbas, A.T., Hassan, A.M., Abdel-dayem, U.A., Qureshi, A.K., Wong, L.-Y.R., Zheng, J., Meyerholz, D.K., Perlman, S., et al. (2022). SARS-CoV-2-Specific Immunoglobulin Y Antibodies Are Protective in Infected Mice. PLoS Pathog. *18*, e1010782. https://doi.org/10.1371/journal.ppat.1010782.

93. Yoshikawa, T., Hill, T., Li, K., Peters, C.J., and Tseng, C.-T.K. (2009). Severe Acute Respiratory Syndrome (SARS) Coronavirus-Induced Lung Epithelial Cytokines Exacerbate SARS Pathogenesis by Modulating Intrinsic Functions of Monocyte-Derived Macrophages and Dendritic Cells. J. Virol. *83*, 3039–3048.

94. Want, E.J., Masson, P., Michopoulos, F., Wilson, I.D., Theodoridis, G., Plumb, R.S., Shockcor, J., Loftus, N., Holmes, E., and Nicholson, J.K. (2013). Global Metabolic Profiling of Animal and Human Tissues via UPLC-MS. Nat. Protoc. *8*, 17–32.

95. Yu, H., Xing, S., Nierves, L., Lange, P.F., and Huan, T. (2020). Fold-Change Compression: An Unexplored But Correctable Quantitative Bias Caused by Nonlinear Electrospray Ionization Responses in Untargeted Metabolomics. Anal. Chem. *92*, 7011–7019.

96. Kessner, D., Chambers, M., Burke, R., Agus, D., and Mallick, P. (2008). ProteoWizard: Open Source Software for Rapid Proteomics Tools Development. Bioinformatics *24*, 2534–2536.

97. Pluskal, T., Castillo, S., Villar-Briones, A., and Oresic, M. (2010). MZmine 2: Modular Framework for Processing, Visualizing, and Analyzing Mass Spectrometry-Based Molecular Profile Data. BMC Bioinf. *11*, 395.

98. Bolyen, E., Rideout, J.R., Dillon, M.R., Bokulich, N.A., Abnet, C.C., Al-Ghalith, G.A., Alexander, H., Alm, E.J., Arumugam, M., Asnicar, F., et al. (2019). Reproducible, interactive, scalable and extensible microbiome data science using QIIME 2. Nat. Biotechnol. *37*, 852–857.

99. Protsyuk, I., Melnik, A.V., Nothias, L.F., Rappez, L., Phapale, P., Aksenov, A.A., Bouslimani, A., Ryazanov, S., Dorrestein, P.C., and Alexandrov, T. (2018). 3D Molecular Cartography Using LC-MS Facilitated by Optimus and 'Ili Software. Nat. Protoc. *13*, 134–154.

100. Wang, M., Carver, J.J., Phelan, V.V., Sanchez, L.M., Garg, N., Peng, Y., Nguyen, D.D., Watrous, J., Kapono, C.A., Luzzatto-Knaan, T., et al. (2016). Sharing and Community Curation of Mass Spectrometry Data with Global Natural Products Social Molecular Networking. Nat. Biotechnol. *34*, 828–837.

101. Nothias, L.-F., Petras, D., Schmid, R., Dührkop, K., Rainer, J., Sarvepalli, A., Protsyuk, I., Ernst, M., Tsugawa, H., Fleischauer, M., et al. (2020).

Feature-Based Molecular Networking in the GNPS Analysis Environment. Nat. Methods *17*, 905–908.

102. Sumner, L.W., Amberg, A., Barrett, D., Beale, M.H., Beger, R., Daykin, C.A., Fan, T.W.-M., Fiehn, O., Goodacre, R., Griffin, J.L., et al. (2007). Proposed Minimum Reporting Standards for Chemical Analysis Chemical Analysis Working Group (CAWG) Metabolomics Standards Initiative (MSI). Metabolomics *3*, 211–221.

103. Kim, H.W., Wang, M., Leber, C.A., Nothias, L.-F., Reher, R., Kang, K.B., van der Hooft, J.J.J., Dorrestein, P.C., Gerwick, W.H., and Cottrell, G.W. (2021). NPClassifier: A Deep Neural Network-Based Structural Classification Tool for Natural Products. J. Nat. Prod. *84*, 2795–2807.

STAR★METHODS

KEY RESOURCES TABLE

REAGENT or RESOURCE	SOURCE	IDENTIFIER
Bacterial and virus strains		
SARS2-N501Y$_{MA30}$	Perlman lab - Wong et al.[28]	N/A
Biological samples		
SARS2-N501Y$_{MA30}$ infected and uninfected mouse lung tissue	This paper	N/A
Chemicals, peptides, and recombinant proteins		
TRIzol Reagent	ThermoFisher	Cat#15596026
Ketamine	Dechra	Cat#NDC59399-114-10
Xylazaine	Dechra	Cat#17033-099-05
Critical commercial assays		
High-Capacity cDNA Reverse Transcription Kit	ThermoFisher	Cat#4368814
SYBR Green real-time PCR master mix	ThermoFisher	Cat#A25778
Deposited data		
Raw data files	This paper	MassIVE: MSV000094591 (https://doi.org/10.25345/C51Z42451)
Code used for analysis	This paper	https://github.com/jarrodRoachChem/covid19
Experimental models: Cell lines		
ACE-2 expressing Calu-3 2B4 cells	Tseng lab - Yoshikawa et al.[93]	N/A
Experimental models: Organisms/strains		
Mouse: C57BL/6J female mice	The Jackson Laboratory	Cat#000664
Oligonucleotides		
Primer: 2019-nCoV_N1-Forward: 5′-GACCCCAAAATCAGCGAAAT-3′	Invitrogen	Cat#10336022
Primer: 2019-nCoV_N1-Reverse: 5′-TCTGGTTACTGCCAGTTGAATCTG-3′	Invitrogen	Cat#10336022
Primer: GADPH-Forward: 5′-AGGTC GGTGTGAACGGATTTG-3′	Integrated DNA Technologies	Cat#19039718
Primer: GADPH-Reverse: 5′-TGTAG ACCATGTAGTTGAGGTCA-3′	Integrated DNA Technologies	Cat#19039718
Software and algorithms		
MSconvert	Kessner et al.[96]	https://proteowizard.sourceforge.io/
MZmine	Pluskal et al.[97]	https://github.com/mzmine/mzmine2/releases
QIIME 2	Caporaso et al.[98]	https://qiime2.org/
‘ili	Protsyuk et al.[99]	ili.embl.de
Global natural products social molecular networking resource	Wang et al.[100]; Nothias et al.[101]	https://gnps.ucsd.edu/ProteoSAFe/static/gnps-splash.jsp
NPClassifier	Kim et al.[103]	https://npclassifier.ucsd.edu/
Other		
Vanquish UHPLC	Thermo Scientific	https://www.thermofisher.com/us/en/home/products-and-services/promotions/industrial/vanquish-hplc-uhplc-systems.html
Q-Exactive Plus Mass Spectrometer	Thermo Scientific	https://www.thermofisher.com/order/catalog/product/IQLAAEGAAPFALGMBDK
Kinetex 1.7 μm C8 100 Å, 50 × 2.1 mm column	Phenomenex	Cat#00B-4499-AN
Fisherbrand Bead Mill 24 Homogenizer	Fisher Scientific	Cat#15-340-163
Fisher Scientific ultra-sonicator	Fisher Scientific	Cat#15337435

EXPERIMENTAL MODEL AND STUDY PARTICIPANT DETAILS

SARS-CoV-2 model

Mice exhibit resistance to ancestral SARS-CoV-2 infection. To allow for murine infection, a point mutation was introduced into SARS-CoV-2 (N501Y), followed by 30 sequential passages in wild-type BALB/c mice as described in Wong et al.[28] This model was extensively characterized in Wong et al.[28] and has been implemented in multiple subsequent studies.[89–92] A brief highlight of key characteristics of the model is provided here. After 30 serial passages through mouse lungs and plaque purification, the modified virus demonstrated increased adaptation and lethality in mice.[28] Sequencing revealed an identical set of mutations between the plaque-purified virus (used for this current study) and the virus from passage 30 mouse lungs. Infectious virus was detected in multiple organs at very low levels at 2 days post-infection, but only persists in the lung at subsequent timepoints. Pathological changes, such as alveolar edema and perivascular infiltration, were detected in lung tissue and the nasal cavity at 2, 4, and 6 DPI, but not in other collected organs. The spike, membrane, and nucleocapsid proteins all elicited $CD4^+$ and $CD8^+$ T cell responses. For more extensive information about the immunological and histological characteristics of this model, refer to Wong et al.[28]

ACE-2 expressing cells derived from male Calu-3 cells, provided by the Tseng lab, were cultured in Dulbecco's modified Eagle's medium (DMEM) supplemented with 20% fetal bovine serum (FBS), 100 U/mL penicillin, and 10 μg/mL streptomycin at 37°C with 5% CO_2. SARS2-N501Y_{MA30} was propagated as described in Yoshikawa et al. after plaque purification.[93] Briefly, 10^6 PFU virus stocks were added to Calu-3 cells pre-cultured in T75 flasks and incubated at 37°C for 48 h. Cells were put through two freeze-thaw cycles and then media collected by pipetting. Collected media was centrifuged at 2000 rpm for 5 min at 4°C to clarify supernatants and remove cell debris. Resulting supernatants were combined and aliquoted on dry ice into 20 μL volumes for regular use. Aliquots were stored at −80°C.

Mouse infection

All vertebrate animal studies were performed under IACUC protocol number 2071795, approved by the University of Iowa Institutional Animal Care and Use Committee. Nine-month-old female C57BL/6J mice were purchased from the Jackson Laboratory, housed in groups of 5, and fed *ad libitum*. All mice were housed in an ABSL3 facility and were assigned to experimental groups based on their cage.

Mice were intranasally inoculated with 1000 PFU (n = 12, sublethal dose) or 5000 PFU (n = 6, lethal dose) of SARS2-N501Y_{MA30} virus in a total volume of 50 μL DMEM. Mock-infected controls were inoculated with 50 μL DMEM (n = 10). All mice were euthanized with ketamine/xylazine (100 mg/kg ketamine/12.5 mg/kg xylazine, Dechra, cat#NDC59399-114-10 for ketamine; 17033-099-05 for xylazine). 6 mice infected with the sublethal dose, and 6 mice infected with the lethal dose were euthanized at day 5 post-infection for lung collection. 6 mice infected with the sublethal dose were euthanized at day 20 post-infection. 5 mock-infected mice were euthanized at day 5 and day 20 respectively as time-matched mock controls. Mouse lungs were harvested and divided into 12 pieces as shown in Figure 3B for metabolic analysis and viral load analysis.

METHOD DETAILS

Metabolite extraction

Samples were snap frozen, weighed and homogenized in LC-MS grade water (10 μL/mg) with steel beads using a Fisherbrand Bead Mill 24 Homogenizer at a speed of 5 m/s for 20 s. 1/10 of the homogenized samples was saved for RNA extraction, while the rest of the volume was extracted for metabolites according to Want et al.[94] Briefly, LC-MS grade methanol was added to each sample for a final concentration of 50%. Samples were homogenized again for 20 s and centrifuged at 16,000xg for 10 min at 4°C. 120 μL of the supernatant (aqueous extract) was collected, dried overnight using a SpeedVac, and then frozen at −80°C until LC-MS analysis. A mixture of dichloromethane and methanol at a ratio of 3:1 (V/V) was added to the aqueous extraction pellet. Samples were homogenized for 20 s and centrifuged at 16,000g for 10 min at 4°C. Similar to the aqueous extract, 120 μL of the organic extract was collected, dried overnight using a SpeedVac, and then frozen at −80°C until LC-MS analysis.

LC-MS/MS data collection

Both the organic and aqueous extracts were resuspended in 75 μL of 50:50 LC-MS grade methanol:water spiked with 2 μM sulfadimethoxine. Samples were sonicated for 5 min at a frequency of 40 kHz using a Fisher Scientific ultra-sonicator. Samples were then centrifuged for 5 min at 12,800xg. 60 μL of the supernatant from the organic and aqueous portions of each sample were combined into a single well of a 96-well plate, resulting in 120 μL volume prior to analysis. Extraction blanks were resuspended in the same way. A pooled quality control (QC) was created by combining 2 μL of each sample. A randomized run sequence was generated through the use of the RAND() function in excel to minimize batch effects. LC analysis was performed using a Kinetex 1.7 μm C8 100 Å, 50 × 2.1 mm column on a Vanquish HPLC (Thermo Scientific). The column temperature was set to 40°C. Mobile phase A was LC-MS grade water (Fisher Optima) with 0.1% formic acid (Fisher Optima, CAS 64-18-6) and mobile phase B was LC-MS grade acetonitrile (Fisher Optima) with 0.1% formic acid. Liquid chromatography gradient parameters, as per,[10] can be found in Table S6. MS/MS analysis was performed using a Q-Exactive Plus (Thermo Scientific) high resolution mass spectrometer

with the parameters found in Table S7, as per.[10] Prior to MS/MS analysis, the instrument was calibrated using Pierce LTQ Velos ESI positive ion calibration solution (Thermo Scientific; cat# 88322). A 2, 5, 10, 20, and 30 μL volume of the QC was injected to determine the ideal injection volume for these samples.[95] By examining the linearity of the signal intensity and peak shape of internal standards and metabolites of interest as well as the overall signal intensity of the sample, a sample injection volume of 5 μL was determined to be the optimal injection volume. 5 μL of a blank and QC were injected between every 12 samples to monitor batch effects and signal drift. A mixture of 6 internal standards were injected at the start of the run, approximately every 100 samples, and at the conclusion of the run to monitor column health. No signs of batch effects or column deterioration were observed during the course of the run.

QUANTIFICATION AND STATISTICAL ANALYSIS

Viral load analysis

To quantify the titers of SARS-CoV-2 in the indicated sections of lungs from mock-infected and infected mice, 1/10 volume of homogenized samples was collected for RNA extraction by using TRIzol Reagent (Invitrogen, cat#15596018) according to the manufacturer's instructions. 0.2 μg total RNA were converted to cDNA using High-Capacity cDNA Reverse Transcription Kit (ThermoFisher, cat#4368814). RT-qPCR was conducted using SYBR Green real-time PCR master mix (ThermoFisher, cat#A25778) in 20 μL reactions using standard reaction conditions (Hold stage: 50°C 2min, 95°C 10min; PCR stage: 95°C 15 s, 60°C 1 min, repeat for 40 cycles; Melt curve stage: 95°C 15 s, 60°C 1 min, 95°C 15 s). Average values from duplicates were used to calculate the relative abundance of transcripts normalized to mouse GAPDH and presented as $2^{-\Delta\Delta CT}$. The primers used for amplification of viral N transcript, as per,[28] were synthesized and purchased from Invitrogen (Cat#10336022) and were as follows: 2019-nCoV_N1-F:5′-GACCCCAAAATCAGCGAAAT-3′; 2019-nCoV_N1-R: 5′-TCT GGTTACTGCCAGTTGAATCTG-3′. The primers used for amplification of GAPDH were purchased from Integrated DNA Technologies (IDT #19039718) and were as follows: GADPH F: 5′-AGGTCGGTGTGAACGGATTTG-3'; GADPH R: 5′-TGTAGAC CATGTAGTTGAGGTCA-3'.

Raw data processing

Following data collection, raw spectra were converted into the mzXML format using MSconvert[96] before being analyzed using MZmine 2.53.[97] Parameters for MZmine were adjusted by manually inspecting built chromatograms within the samples for signs of over and under splitting. A full list of parameters can be found in Table S8. Metabolites present in the blank that lacked an average signal intensity greater than 3 times the intensity of the metabolite in the lung samples were removed. Signal intensity was then normalized using the Total Ion Current (TIC) normalization method.

Data analysis

QIIME 2[98] was used to perform all calculations related to the Principal Coordinate Analysis. Distance matrices were calculated using "diversity beta" with the Bray–Curtis dissimilarity method on the TIC-normalized MS1 data. PCoAs were generated with "diversity pcoa" and visualized with "emperor plot". Pseudo-F values were calculated based on the Bray-Curtis distance matrices at each position using "beta diversity group significance". 6 samples were identified as outliers and removed from further analysis as they clustered away from all other samples and clustered tightly with internal standard mixtures.

All visualizations of the lung were generated using 'ili,[99] on the lung model generated in.[10]

Feature-based molecular networking was performed using the global natural products social molecular networking resource (GNPS).[100,101] A full list of parameters used to perform FBMN can be found in Table S9, as per.[10] Level 2/3 metabolite annotations (as outlined in the Metabolomics Standards Initiative rankings[102]) were achieved through the use of FBMN and manual inspection of mirror plots to ensure a quality match of MS2 spectra. Level 1 metabolites annotations were assigned by matching retention times of each annotation with LC-MS grade analytical standards using the same column and LC gradient. A full list of metabolite annotation confidence levels for each metabolite mentioned can be found in Table S1.

Chemical families were assigned using annotations and FBMN. Canonical SMILES for annotated metabolites were identified using NPClassifier.[103] A general family assignment was given to all members of each FBMN family based on the annotated metabolites present in each FBMN family. For annotated metabolites with statistical significance, families were manually validated.

Statistical analysis

Statistical parameters for each figure can be found in the legend of the figure. All statistical analysis was performed using R version 4.1. To determine statistical significance between two groups, groups were first tested for normality using the shapiro.test() function in version 4.1.2 of the "stats" package in R. The t.test() function was used to compare two normally distributed groups while non-normally distributed groups were tested with wilcox.test(). Correlation analysis was performed using the Spearman method in the cor.test() function in version 4.1.2 of the "stats" package in R. False-discovery-rate adjusted *p*-values were generated from the entire list of *p*-values in each analysis using the p.adjust() function with the "fdr" method in version 4.1.2 of the "stats" package in R. Violin plots and boxplots were generated using version 3.4.3 of "ggplot2". χ^2 values were generated using the chisq.test() function in

base r. For chi-squared calculations, the expected distribution for upregulated versus downregulated was 0.5 and 0.5. For all tests, a *p*-value of less than 0.05 or an FDR-adjusted *p*-value of less than 0.05 in the event of multiple comparisons was defined as a significant result.

For comparisons between central and peripheral lung tissue, the TIC-normalized signal intensity for each metabolite in the infected tissue was divided by median value of the TIC-normalized signal intensity of the metabolite in the central and peripheral lung tissue time-matched mock-infected control, respectively.